DEVELOPMENT OF A HUMAN STEM CELL-DERIVED, HYDROGEL-BASED BLOOD-BRAIN BARRIER MODEL TO INVESTIGATE THE LIMITED BRAIN DELIVERY OF IMMUNOGLOBULIN G

by

John S. Ruano-Salguero

A dissertation submitted to the Faculty of the University of Delaware in partial fulfillment of the requirements for the degree of Doctor of Philosophy in Chemical Engineering

Fall 2020

DEVELOPMENT OF A HUMAN STEM CELL-DERIVED, HYDROGEL-BASED BLOOD-BRAIN BARRIER MODEL TO INVESTIGATE THE LIMITED BRAIN DELIVERY OF IMMUNOGLOBULIN G

by

John S. Ruano-Salguero

Approved: _____
Eric M. Furst, Ph.D.
Chair of the Department of Chemical and Biomolecular Engineering

Approved: _____
Levi T. Thompson, Ph.D.
Dean of the College of Engineering

Approved: _____
Louis F. Rossi, Ph.D.
Vice Provost for Graduate and Professional Education and Dean of the Graduate College

I certify that I have read this dissertation and that in my opinion it meets the academic and professional standard required by the University as a dissertation for the degree of Doctor of Philosophy.

Signed: _____

Kelvin H. Lee, Ph.D.
Professor in charge of dissertation

I certify that I have read this dissertation and that in my opinion it meets the academic and professional standard required by the University as a dissertation for the degree of Doctor of Philosophy.

Signed: _____

Wilfred Chen, Ph.D.
Member of dissertation committee

I certify that I have read this dissertation and that in my opinion it meets the academic and professional standard required by the University as a dissertation for the degree of Doctor of Philosophy.

Signed: _____

April M. Kloxin, Ph.D.
Member of dissertation committee

I certify that I have read this dissertation and that in my opinion it meets the academic and professional standard required by the University as a dissertation for the degree of Doctor of Philosophy.

Signed: _____

John H. Slater, Ph.D.
Member of dissertation committee

ACKNOWLEDGMENTS

To the many mentors, peers, family, and friends that have helped and supported me through this exciting but daunting time, I thank you so very much. Although I may not have the time (or space) to mention you all, I appreciate the fond memories.

Foremost, I would like to thank my advisor Kelvin Lee for his guidance, patience, and support. It is not often that a graduate student is privileged to be 'in the driver's seat,' so I appreciate your encouragement that started on day one. I hope to emulate your example and teachings throughout my career.

I extend my thanks to my committee members Profs. April Kloxin and Wilfred Chen for their input and suggestions throughout our formal and informal meetings. I thank my committee member and collaborator Prof. John Slater for his advice and commitment to my success. I would also like to thank Prof. Jong Youn Baik for his friendship, mentorship, and support. Lastly, I would certainly be remiss to not thank Leila Choe and the many current and former members of the Lee group. From the group outings, Friday ho-ho's, and lunch breaks, it has been my pleasure to know you all.

Finally, I give my deepest thanks to my family. Angie, I cannot begin to express all the appreciation and admiration I feel for my greatest supporter, best friend, and 'co-PI.' You have brought so much joy into my life, and I am so grateful for the many ways you brighten my day. Thank you from the bottom of my heart, my dearest wife. To my extended family, the Norton's and Piccinotti's, thank you for

embracing me so warmheartedly. I am blessed to call you all family. To my dearest mother and father, I am forever grateful for your encouragement and support that has taken me to where I am. You both have always inspired me to do my best and work my hardest. To my siblings, Chris and Marcy, thank you for always being there for me.

TABLE OF CONTENTS

LIST OF TABLES

LIST OF FIGURES

ABSTRACT

Immunoglobulin G (IgG)-based immunotherapies hold tremendous promise as the first disease-modifying treatment for Alzheimer's disease and related dementias. However, the poor brain delivery of IgG (~0.01% of the administered dose) necessitates unprecedented dosing regimens that raise concerns about treatment cost and accessibility. Efforts to improve the penetrance of bloodborne IgG into the brain have attempted to identify the intracellular processes governing IgG transport across the restrictive vasculature of the brain (termed the blood-brain barrier (BBB)). Despite numerous studies, the difficulty of performing cellular-level characterizations on the BBB *in vivo* have led to conflicting findings. To this end, the objective of this thesis is to investigate the processing and transport of IgG at the BBB by using cellular-level *in vitro* characterizations.

Initially, an *in vitro* approach capable of simultaneously visualizing and quantifying IgG transport across the brain endothelial cells (BECs) that form the BBB was developed. Previous work from our group demonstrated the utility of induced pluripotent stem cell-derived BEC-like cells (termed iBECs) to study IgG transport, however experimental limitations of the cell culture inserts traditionally used to construct *in vitro* BBB models hindered further investigation. Here, a collagen type I (COL1) hydrogel was coupled with iBECs to establish an *in vitro* BBB model

amendable with live-cell fluorescence microscopy. The resultant hydrogel-based BBB model and microscopy-based transport quantification method were validated with proteomic and functional comparisons to benchmark data previously reported for iBECs on cell culture inserts. The easy-to-construct COL1-based BBB model presented here is the first to enable the visual and quantitative assessment of molecular transport across BECs at nanomolar concentrations.

Evidence suggests that IgG-specific processing occurs within BECs, but any influence on transport remains unclear. Here, the involvement of the neonatal Fc receptor (FcRn), which can salvage internalized IgG away from lysosomes and back to the luminal cell surface (i.e. recycling) or shuttle internalized IgG to the abluminal cell surface (i.e. transcytosis), was investigated by comparing the transport and processing of IgGs that are recognized or unrecognized by FcRn. Using super-resolution fluorescence microscopy, the two IgGs demonstrated differences in lysosomal accumulation consistent with FcRn-mediated recycling. Yet, IgG transport rates were independent of FcRn engagement or concentration, indicating that while FcRn can recycle IgG at the BBB, it does not influence its transcytosis. Complementary studies with macromolecules ranging in molecular weight (12-155 kDa) demonstrated comparable transport rates to IgG (150 kDa), suggesting concentration/size-independent fluid-phase endocytosis and nonspecific transcytosis events as the basis for IgG and most macromolecular transport at the BBB. Indeed, only macromolecules leveraging receptor-mediated or adsorptive endocytosis mechanisms exhibited faster transport rates in a concentration or charge-dependent manner, respectively. The

ability of adsorptive endocytosis to improve IgG transport was demonstrated via the conjugation of negatively-charged fluorescent probes; however, alterations in FcRn-mediated recycling were detected and were attributed to indirect inhibition of FcRn engagement within endosomes as conjugated/unconjugated IgG exhibited comparable FcRn-IgG binding in solution.

Collectively, these findings highlight the utility of *in vitro* BBB models to characterize and screen therapeutics, shed light on the factors influencing the transport of IgG across the BBB, and provide possible routes to engineer improved IgG variants with enhanced BBB penetrance.

Chapter 1

INTRODUCTION

1.1 Motivation and Background

1.1.1 Challenges in Developing Dementia Treatments

Unlike the mild and gradual cognitive decline associated with normal aging, those with dementia experience rapid and debilitating cognitive impairment. Though the forms of dementia encompass several neuropathological conditions (e.g. Alzheimer's disease (AD), which represents 60-70% of cases) and clinical symptoms (e.g. memory or motor deficits), an increasing reliance on personalized care and development of comorbidities are typical outcomes of dementia progression. Accordingly, the necessity of full-time care and a decreased quality of life place an untold economic and emotional burden on dementia patients, their caregivers, and society. For example, while the healthcare costs for the 5.8 million Americans with AD totaled $305 billion in 2018, the associated costs for unpaid hours of support by caregivers (often relatives to the patient) was an estimated $244 billion (The Alzheimer's Association 2020). Likewise, it was estimated that AD-induced comorbidites (often pneumonia) contributed to >500,000 deaths for those >75 years of age during 2017, which was additional to the 122,019 deaths attributed directly to AD (The Alzheimer's Association 2020). Despite the vast impacts of dementia on patients and society, symptom management remains the standard of care and the development

of disease-modifying therapies that can halt dementia progression remains an urgent unmet medical need.

An improved understanding of the pathophysiology that underpins dementia onset and progression has identified proteinopathy treatment as a potential disease-modifying approach. The progression of dementia has been linked to the aggregation of misfolded amyloid proteins into insoluble amyloid fibrils that propagate throughout the brain, i.e. a proteinopathy (Golde et al. 2013). Although the exact events that trigger dementia-related proteinopathies remain enigmatic for nonhereditary cases, the amyloidic nature and associated neurotoxicity of the misfolded proteins – tau, amyloid beta, alpha-synuclein, and TDP-43 – indicate similar pathological phenomena (Soto and Pritzkow 2018). Moreover, despite originating from either a central (e.g. neuroinflammation) or peripheral insult (e.g. stroke), most dementias present with one (or more) proteinopathy, i.e. mixed dementia. For example, recent studies indicate >90% prevalence of tau proteinopathy in late-stage patients irrespective of the clinically diagnosed dementia type (e.g. vascular dementia) or presence of other proteinopathies (Kapasi, DeCarli, and Schneider 2017). Given the apparent link between proteinopathy propagation and dementia progression, it is now recognized that current FDA-approved medications, which only promote neuronal function, are unable to modify the rate of cognitive decline (Long and Holtzman 2019). Accordingly, new therapeutic approaches for dementia focus on halting the underlying proteinopathy.

The antagonization of amyloid fibrils with therapeutic immunoglobulin gamma (IgG) antibodies are demonstrating promise in modifying the progression of various dementias, but perspective costs raise unresolved concerns of treatment feasibility and

accessibility. With numerous FDA approvals, the utility of IgGs to bind targets with high specificity – attributable to the antigen-binding fragment (Fab) region – and initiate immune responses – via the fragment crystallizable (Fc) region – has been harnessed for various therapeutic applications (Walsh 2018). Consequently, IgGs against dementia-related amyloidic proteins have been thoroughly investigated by academic and industrial groups to treat dementia by antagonizing fibrillation (Long and Holtzman 2019). Yet, despite nearly 20 years of development, a therapeutic IgG for a dementia indication – mild-cognitive impairment associated with AD – has only recently begun filing with the FDA for a biologics license application (Howard and Liu 2020). A key advancement in achieving the first FDA application, which does not imply FDA approval, has been the recognition that the underlying proteinopathy requires an early intervention, as late-stage patients exhibit multiple copathologies that are self-sustaining and independent of the proteinopathy (Golde et al. 2013). However, given the intrinsic aggregation propensity of amyloidic proteins, an early intervention necessitates a sustained treatment course, potentially spanning 20-40 years post-diagnosis, otherwise the proteinopathy may renew propagation (Golde, DeKosky, and Galasko 2018). While early and sustained IgG treatment is feasible when the therapeutic target resides in the periphery (e.g. immunosuppression), IgGs do not readily reach targets within the brain – with an estimated brain delivery of 0.0001% the injected dose (Kumar et al. 2018). The poor brain penetrance of IgGs has been linked to the limited efficacy observed in several unsuccessful clinical trials, which subsequently led to escalations in IgG doses to unprecedented levels (Long and Holtzman 2019). Thus, combined with the necessity of sustained intervention, the large dose requirements have led to concerns of the associated treatment costs (Golde

2014). In an effort to reduce doses, investigations to understand the limited brain penetrance of IgGs have focused on the cerebral microvasculature, known as the blood-brain barrier (BBB), that regulates the transport of molecules between the blood and brain.

1.1.2 Transport Across the BBB

To maintain a chemical environment suitable for proper neuronal function, the BBB regulates the transport of bloodborne molecules into the brain by exhibiting a permselective phenotype unique from peripheral vasculature. Perivascular and neuronal cells – pericytes, astrocytes, microglia, and neurons – stabilize and confer the unique and restrictive phenotype observed in cerebral endothelium (Zhao et al. 2015), however the exact cues and crosstalk between the BBB and these supportive cells remain elusive. At the cellular level, the brain endothelial cells (BECs) that form the BBB express a myriad of transporters and efflux pumps to actively transport nutrients (e.g. glucose transporter 1 or AOT) or expel nonspecifically internalized small molecules (e.g. MDR1/P-gp), respectively. Additionally, BECs form a complex network of adherent and tight junctions along cell-cell boundaries to restrict nonspecific paracellular transport of molecules <200 Daltons (Da) (Pardridge 2012). To restrict the transcellular transport of large molecules (i.e. transcytosis), BECs upregulate a transmembrane lipid flippase – major facilitator superfamily domain containing 2A (Mfsd2a) – that reduces nonspecific endocytosis (i.e. macropinocytosis), which is widespread in peripheral endothelium and leads to fenestrations (Ayloo and Gu 2019). Yet, the active transcytosis of proteins and other macromolecules across BECs can occur via nonspecific or specific routes (Goulatis and Shusta 2017). For example, membrane-bound receptors on the luminal surface of

BECs trigger the receptor-mediated transcytosis (RMT) of specific proteins or peptides. In contrast, adsorptive interactions between the luminal BEC surface and highly charged (i.e. isoelectric point (pI) >9) proteins or macromolecules results in nonspecific luminal accumulation, leading to higher BEC penetrance. Accordingly, unless an active mechanism (e.g. transporters or RMT receptors) mediates transport across BECs, virtually all small molecule drugs and biopharmaceuticals do not enter the brain at appreciable levels (Pardridge 2012).

Conflicting studies indicate IgG transport across BECs occur either through nonspecific or active processes, which underscores the uncertain influence of the neonatal Fc receptor (FcRn). In contrast to the surface-bound Fc receptors on leukocytes that mediate immune signaling, FcRn only exhibits an affinity to IgG in acidic environments (pH <6) and functions by shuttling endocytosed IgG to the luminal or abluminal membrane of endo- and epithelium (Ward and Ober 2018). FcRn-IgG interactions occur predominately in the endothelium that forms the vast peripheral vasculature and results in the extended serum half-life of bloodborne IgG by reducing IgG catabolism (i.e. lysosomal degradation). FcRn diverts the shuttling of IgG to lysosomes by engaging endocytosed IgG within early endosomes (pH 5.5) and subsequently releasing the bound IgG back to the vascular lumen (pH 7.4) during endosomal-luminal membrane fusion. Interestingly, undetermined tissue-specific cues can enable FcRn to mediate IgG transcytosis, such as the transfer of maternal IgG across placental epithelium to the offspring, hence the neonatal nomenclature (Pyzik et al. 2019). With respect to BECs, FcRn knock-out studies in mice have demonstrated no change in IgG penetrance into the brain – as measured by the ratio of IgG in the cerebrospinal fluid (CSF) relative to serum (Abuqayyas and Balthasar 2013).

Similarly, the brain penetrance of either endogenous or exogenous IgG in naive mice are comparable with other serum proteins (Wang et al. 2018). Taken together, it is hypothesized that IgG and other macromolecules exhibit a low rate of nonspecific transport across BECs (Yu and Watts 2013). However, several studies have challenged the notion that IgG transport does not involve active processing by BECs (Zlokovic et al. 1990). For example, when the confounding influence of endogenous IgGs was eliminated by performing *in situ* brain perfusions with exogenous IgGs in a buffered saline, the uptake rate of IgG into the brain exhibited saturable behavior and suggested that BECs can actively transport IgG at low concentrations (St-Amour et al. 2013). Likewise, *ex vivo* analysis of intracellular IgG processing within BEC have led to hypotheses that recycling or lysosomal degradation indirectly influence IgG transport (Villasenõr et al. 2016). Accordingly, controlled experimental conditions, kinetic characterizations, and cellular-level analysis have been proposed to address the uncertainty regarding IgG transport across BECs, which are facilitated by *in vitro* models.

1.1.3 *In vitro* BBB Models

Traditionally, *in vitro* models of the BBB have been implemented to elucidate transport pathways and screen therapeutics. The identification of various RMT receptors and nutrient transporters through *in vivo* investigations have been complemented with *in vitro* studies to characterize substrate selectivity and saturable conditions (Pardridge 1998). Coupled with cellular-level characterizations, *in vitro* studies have also unraveled the intracellular pathways that hinder or facilitate transport (Villaseñor et al. 2019). With respect to therapeutic screening, the rate of transport – often reported as a permeability value – of both benchmarked molecules and

therapeutic candidates are ranked and correlated to *in vivo* data. Generally, confluent monolayers of immortalized or primary BECs enable sufficient correlations, but co- and tri-cultures with perivascular or neuronal cells have demonstrated improvements, particularly for substrates of efflux pumps (Pardridge 2020). Either for transport characterizations or therapeutic screening, proteomic and transcriptomic studies indicate that BBB models derived from human sources provide human-specific transporter, efflux pump, and RMT selectivity as well as expression levels (Uchida et al. 2011). However, an inherent issue with all primary or immortalized BECs are high rates of para- and transcellular transport, evidenced by low transendothelial electrical resistance (TEER) and high macromolecular permeability values, respectively (Helms et al. 2015). Accordingly, the identification of human BECs sources with relevant barrier properties has remained a challenge.

As an alternative to primary or immortalized BECs, the differentiation of human induced pluripotent stem cells (iPSCs) to BEC-like cells (iBECs) represent the state-of-the-art in modeling the human BBB. Although the derivation of BEC-like cells from pluripotent and multipoint stem cells have been reported, protocols that co-differentiate endothelial and neuronal progenitors produce cells with a robust BBB phenotype, e.g. iBECs (Aday et al. 2016). Coupled with high proteomic and transcriptomic correlations to human BECs, functional evaluations of iBECs have demonstrated TEER and permeability values of benchmark small molecules that are comparable to those of the rodent BBB *in vivo* (Mantle, Min, and Lee 2016). Accordingly, iBECs have emerged as ideal candidates to replace primary and immortalized human BECs, and have the capability to facilitate personalized *in vitro* modeling as patient-derived iPSCs become democratized (Workman and Svendsen

2020). With respect to IgG and transcellular transport, comparable permeability values between iBECs and the *in vivo* rat BBB indicate iBECs exhibit both low paracellular leakage (i.e. sufficient tight junction formation) and limited vesicular activity (Mantle, Min, and Lee 2016; Kutuzov, Flyvbjerg, and Lauritzen 2018). However, the low rates of transcellular transport across iBECs have necessitated high analyte concentrations and long assay times due to constraints from traditional experimental platforms (Mantle, Min, and Lee 2016), which impede the study of IgG transport across BECs.

Despite the utility and high-throughput capability of well-established insert-based experimental systems that examine BEC transport, several limitations have necessitated the development of alternative systems. Cell culture inserts are ideal platforms to culture and assay the barrier functionality of endo- and epithelium, and have remained quintessential *in vitro* models of the BBB since the early 1990's (Joó 1992). To mimic the separation of blood and brain across the BBB, two aqueous compartments are partially separated across a confluent BEC monolayer that forms on the rigid but porous membrane of a cell culture insert. To assay transport, an analyte is added in the upper (i.e. luminal) compartment above the polarized BEC monolayer and its accumulation into the bottom (i.e. abluminal) compartment is subsequently quantified at multiple timepoints. Although facile to perform, the analysis of transport using insert-based BBB models is hampered by experimental difficulties and limitations, such as the influence of porous membrane properties or the inability to visualize transport *in situ*. As an alternative, new BBB models leverage the advancements from tissue engineering efforts and replace inserts with natural/synthetic hydrogels that serve as both a rigid/porous platform and an abluminal compartment. The opaque properties of hydrogels derived from collagen type I

(COL1) or polyethylene glycol (PEG) – combined with fluorescence microscopy have enabled the real-time visualization and quantification of transport across BECs, including iBECs. However, based on the construction of the hydrogel-based systems (i.e. large hydrogel volumes), the quantification of slow transport rates for macromolecules has not yet been demonstrated (Grifno et al. 2019; Seo, Motallebnejad, and Azarin 2020). Therefore, the engineering of hydrogel-based *in vitro* BBB models that are able to quantify the slow rates of transcellular iBEC transport are needed to address the outstanding questions regarding IgG transport at the BBB.

1.2 Project Goals

The purpose of this work is to develop a hydrogel-based *in vitro* BBB model that enables the assessment of intracellular processing and cellular permeability and apply the model to study IgG transport across iBECs.

To accomplish this work, two objectives were satisfied:

(1) *Establish a hydrogel-based* in vitro *BBB model for simultaneous iBEC permeability quantification and intracellular visualization*: To quantify and visualize the transport of analytes across iBECs, a hydrogel-based analog to traditional insert-based experimental systems was developed to leverage live-cell fluorescence microscopy. The development, validation, and benchmarking of the hydrogel-based iBEC model and live-cell microscopy-based transport assay is detailed in Chapter 2.

(2) *Probe the processing and transport of IgG by iBECs*: To address the relationship between processing and transport, super-resolution microscopy-based methods to quantify the intracellular accumulation and lysosomal compartmentalization of endocytosed analytes were developed to complement

transport quantification via live-cell microscopy. In Chapter 3, the influence of FcRn-mediated processes on IgG transport is directly examined and complemented with comparative studies using macromolecules of varying size and transport pathways. Building upon the discoveries of native IgG-BEC interactions, the overlooked changes in processing and transport that can occur following the fluorescent labeling of IgG is characterized in Chapter 4.

Chapter 2

EFFLUX PUMP SUBSTRATES SHUTTLED TO CYTOSOLIC OR VESICULAR COMPARTMENTS EXHIBIT DIFFERENT PERMEABILITY IN A QUANTITATIVE HUMAN BLOOD-BRAIN BARRIER MODEL

2.1 Preface

This chapter is adapted from: Ruano-Salguero JS and Lee KH. (2018) Efflux pump substrates shuttled to cytosolic or vesicular compartments exhibit different permeability in a quantitative human blood–brain barrier model, with permission (see Appendix D).

This chapter describes the construction and application of a COL1 hydrogel as an engineered alternative to traditional insert-based BBB models. After confirming the formation of confluent iBEC monolayers on a low volume (3-7 µL) COL1 hydrogel, a live-cell fluorescence microscopy-based approach to quantify the permeability of small and large molecules, including IgG, at low concentrations (nM-µM) was developed and validated. A benchmarking of iBEC performance on the COL1 hydrogel was performed with proteomic and functional assessments, and the utility of coupling permeability measurements with intracellular visualizations was demonstrated with two small molecules often used to assess paracellular leakage.

The authors thank Dr. Jeffrey L. Caplan at the Delaware Biotechnology Institute Bioimaging Center for assistance with confocal microscopy. The authors also thank Dr. John H. Slater at the University of Delaware for helpful discussions. This work was funded in part by a NSF GRFP fellowship (Award Number 1247394).

Microscopy access was supported by grants from the NIH-NIGMS (P20 GM103446), the NSF (IIA-1301765) and the State of Delaware.

2.2 Abstract

Representative *in vitro* blood-brain barrier (BBB) models can support the development of strategies to efficiently deliver therapeutic drugs to the brain by aiding the characterization of their internalization, trafficking, and subsequent transport across the BBB. A collagen type I (COL1) hydrogel-based *in vitro* BBB model was developed to enable the simultaneous characterization of drug transport and intracellular processing using confocal microscopy, in a way that traditional insert-based *in vitro* BBB models cannot. Human induced pluripotent stem cells (hiPSCs) were differentiated into cells that exhibited a BBB-like phenotype on COL1 hydrogels, which included the expression of key BBB-specific proteins and low permeability of representative small and large molecule therapeutics. Furthermore, the BBB-phenotype observed on the COL1 hydrogel was similar to that previously reported on porous inserts. The intracellular visualization of two small molecule efflux pump substrates within the hiPSC-derived BBB-like cells demonstrated a difference in cytosolic and vesicular accumulation, which complemented permeability measurements demonstrating a difference in transport rate. The easy-to-construct COL1-based hiPSC-derived BBB model presented here is the first *in vitro* two-dimensional BBB experimental system that enables the simultaneous quantification of cellular permeability and visualization of intracellular processes by utilizing confocal microscopy, which can provide insights regarding the relationship between transport and intracellular trafficking of therapeutic drugs.

2.3 Introduction

The blood-brain barrier (BBB) is the continuous cerebral endothelium that regulates the transport of molecules between the bloodstream and the central nervous system. The brain microvascular endothelial cells (BMECs) that constitute the BBB express a unique set of nutrient transporters and efflux pumps to maintain a chemical environment suitable for neuronal function (Daneman 2012). To restrict the entry of foreign or potentially neurotoxic molecules, BMECs form nearly impermeable cell-cell connections via tight junctions (Bauer et al. 2014) and suppress the vesicular transport characteristic of endothelium in the periphery (Andreone et al. 2017). Accordingly, the BBB poses an obstacle to the treatment of brain diseases by restricting the delivery of both small and large molecule therapeutics into the brain (Pardridge 2012). Improved knowledge of the cellular mechanisms regulating the transport of therapeutics across the BBB could help lead to improved strategies for efficient brain delivery (Goulatis and Shusta 2017; Huang and Mucke 2012; Gabathuler 2010). Although *in vivo* and *ex vivo* animal models help elucidate potential transport pathways at the BBB (Villasenõr et al. 2016; Weber et al. 2018), a complete description of the dynamic transport processes at the cellular level is not readily obtainable with existing technology. *In vitro* models of the BBB are complementary tools that can provide additional cellular-level information of transport processes and aid in the screening of emerging therapeutic candidates (Villaseñor et al. 2017; Ribecco-Lutkiewicz et al. 2018).

Traditionally, *in vitro* models of the BBB have relied on BMECs derived from primary or immortalized animal and human sources (Helms et al. 2015; Wuest and Lee 2012; Wuest, Wing, and Lee 2013). Human-derived *in vitro* BBB models are preferable over comparable animal-derived models given the well-established

differences in the expression of key transporter proteins between animal and human BMECs (Warren et al. 2009). However, primary and immortalized BMECs do not exhibit barrier functionality comparable to an *in vivo* BBB. Recently, human induced pluripotent stem cell-derived BMECs (hiPSC-BMECs) have emerged as a superior alternative, with reported transendothelial electrical resistance (TEER) values as high as 2500-3000 $\Omega \cdot cm^2$ (Mantle, Min, and Lee 2016; Qian et al. 2017), which are comparable to the benchmark 1500-6000 $\Omega \cdot cm^2$ value observed *in vivo* in rats (Butt, Jones, and Abbott 1990). Additionally, these BBB-like cells express key tight junction proteins, transporters, and efflux pumps and also exhibit low permeability of small and large molecules (Mantle, Min, and Lee 2016). Although hiPSC-BMECs represent a significant advancement in the modeling of the BBB *in vitro*, similar advancements in the experimental systems used to construct *in vitro* BBB models can enable studies that provide a thorough characterization of transport across BMECs.

Over the past three decades, *in vitro* BBB models have predominately used an insert-based experimental system due to commercial availability, high throughput potential, and ease of use (Joó 1992). In this experimental system, BMECs are grown on a porous insert that separates a luminal and abluminal compartment, which represent the bloodstream and brain, respectively. The transport of molecules across the monolayer of BMECs is quantified by measuring the concentration of analytes in both compartments over time (Siflinger-Birnboim et al. 1987). However, these insert-based systems do not allow for direct visualization of transport processes within BMECs, and complementary intracellular studies on different experimental systems, such as glass coverslips, are not routinely characterized. Recently, tissue-engineered systems using a hydrogel-forming matrix have enabled the construction of perfusable

three-dimensional vessels that mimic the vascular nature of the BBB and enable the visualization and quantification of transport across BMECs (Hopkins et al. 2015). Although these three-dimensional models have substantial potential to advance the modeling of the BBB *in vitro*, they have not been widely adopted due to disadvantages such as complexity of construction and difficulty of forming intact lumens, especially when using hiPSC-BMECs (Katt et al. 2018). Accordingly, two-dimensional hydrogel-based systems, which are analogous to the insert-based experimental system, are comparable alternatives that are facile to construct and still enable the ability to monitor transport across cells (Huynh et al. 2011). However, these two-dimensional hydrogel-based systems have not yet been applied to generate an *in vitro* model of the BBB, and previous reports using such systems did not detail methods to quantify absolute measurements of transport, such as permeability, that are useful to establish meaningful comparisons between *in vitro* and *in vivo* observations.

In this work, we developed a new two-dimensional hydrogel-based BBB model using hiPSC-BMECs and collagen type I (COL1) that is simple to construct and enables both intracellular visualization and quantification of molecular transport, and applied it to characterize the transport of representative small and large molecule therapeutics. First, we demonstrate that hiPSC-BMECs can be cultured on COL1 hydrogels to form a confluent cellular monolayer that expresses key BBB-relevant proteins. Confocal microscopy was used to quantify the permeability of benchmark small and large molecules to verify hiPSC-BMEC monolayers on COL1 hydrogels exhibit BBB-like barrier function. Additionally, we found that hiPSC-BMECs exhibit a loss in both small and large molecule barrier function with increasing culture age, which was not attributed to a loss in monolayer confluence. Finally, we highlight the

importance of visualizing intracellular processes by observing a difference in intracellular accumulation and transport between two small molecule probes used to assess efflux pump activity.

2.4 Methods

2.4.1 Preparation of COL1-based Experimental System

COL1 from rat tendon (Corning, Corning, NY) was obtained in 0.02 N acetic acid at varying concentrations (8-11 mg/ml). A 5 mg/ml COL1 solution was prepared according to the manufacturer's protocol. 8-chambered glass coverslips (Cellvis, Mountain Veiw, CA) underwent functionalization a day before COL1 conjugation. First, the glass was silanized by incubating 10% (v/v) (3-aminopropyl)-trimethoxysilane (Sigma-Aldrich, St. Louis, MO) in ethanol for 15 minutes. Following aspiration, carboxylic groups were incorporated by immediately incubating with 0.1 M succinic acid (Sigma-Aldrich) in ethanol overnight. Similarly, after the aspiration of succinic acid, 200 mM of ethyl(dimethylaminopropyl) carbodiimide (EDC; Thermo Fisher Scientific, Waltham, MA) and N-hydroxysuccinimide (NHS; Thermo Fisher Scientific) in pH 4.7 BupH 2-(N-morpholino)ethanesulfonic acid buffered saline (Thermo Fisher Scientific) was directly added to activate the newly introduced carboxylic groups. The EDC/NHS solution was incubated for at least 15 minutes before thorough aspiration. Subsequently, the EDC/NHS activated 8-chambered glass coverslip was placed on an ice pack within a sterile cell culture hood where 4 μL (unless specified otherwise) of cold COL1 solution was added to the chilled glass surface. It is important not to allow a substantial amount of the COL1 solution to touch the sides of the chambers, as the COL1 solution will move towards the sides

during gelation. Following addition of the COL1 solution, the 8-chambered glass coverslip was incubated at 37 ºC for at least 1 hour to allow complete COL1 gelation. Finally, the COL1 hydrogels were rehydrated in warm endothelial cell medium (EC-) consisting of human endothelial cell serum-free medium (Life Technologies, Carlsbad, CA) supplemented with 1% platelet-poor derived serum (Alfa Aesar, Tewksbury, MA).

2.4.2 hiPSC Differentiation and Subculture on COL1 Hydrogels

IMR90-4 (WiCell, Madison, WI) hiPSCs were maintained on growth factor-reduced Matrigel (Fisher Scientific, Hampton, NH) in mTeSR1 medium (STEMCELL Technologies, Vancouver, BC, Canada) and passaged using ReLeSR (STEMCELL Technologies) as described by the manufacturer. hiPSCs were differentiated to BMECs as previously described (Mantle, Min, and Lee 2016). Fully differentiated hiPSCs were then dissociated into single cells following a 1 hour treatment at 37 ºC using StemPro Accutase (Life Technologies, Carlsbad , CA). The single cell suspension was then diluted (1:5) in EC-, centrifuged at 1000 RPM for 3 minutes, and resuspended in fresh EC-. Cell density was determined using the Trypan blue exclusion method. Subsequently, cells were plated onto preassembled COL1 hydrogels at a density of at least $1x10^6$ cells/cm^2 (Wilson et al. 2015). Media was replaced with warm EC- each day after the initial passage to COL1 hydrogels. All experiments were performed on the second day two after subculture unless noted otherwise.

2.4.3 Quantification of Hydrogel Average Mesh Size

Confocal reflection microscopy (CRM) was used to image the COL1 hydrogel at a high resolution of 0.0519 μm per pixel. Image processing software (Image J, NIH) was used to determine the average size of void space between the COL1 fibers as previously described (Y. L. Yang, Leone, and Kaufman 2009). CRM images were captured with a Zeiss 710 laser scanning confocal microscope equipped with a C-Apochromat water immersion objective (NA 1.2).

2.4.4 Live-cell Confocal Microscopy

Cells were incubated with 5 μM calcein acetoxymethyl blue, a live-cell probe, (CB; AnaSpec, Fremont, CA) for at least 15 minutes and was removed prior to imaging. The 8-chambered glass coverslips were mounted on a heated microscope stage housed in an enclosure maintained at 37 ºC and 5% CO_2. All live-cell images were captured using a Zeiss 710 laser scanning confocal microscope equipped with a C-Apochromat water immersion objective (NA 1.2).

2.4.5 Immunocytochemistry

Cells were fixed with 2% (v/v) paraformaldehyde (Electron Microscopy Sciences, Hatfield, PA) in Dulbecco's phosphate-buffered saline (DPBS; Life Technologies) for 10 minutes. After three washes with DPBS, cells were permeabilized with 0.1% (v/v) Triton X-100 (Sigma-Aldrich) in DPBS for 5 minutes. Cells were incubated with primary antibodies (mouse anti-claudin-5, rabbit anti-occludin, mouse anti-glucose transporter 1; Life Technologies; mouse anti-p-glycoprotein; Fisher Scientific; rabbit anti-major facilitator superfamily domain-containing protein 2A; Abcam, Cambridge, MA) at a concentration of 3 μg/ml in DBPS for 1 hour at room temperature. After three DPBS washes, cells were incubated

for 1 hour with 6 μg/ml of the corresponding secondary antibody (Alexa Fluor 488 conjugated goat anti-rabbit or goat anti-mouse; Life Technologies) in DPBS for 1 hour at room temperature. Immunocytochemistry was performed on cells at day two after subpassage to COL1 hydrogels, and imaged with a Zeiss 710 laser scanning confocal microscope equipped with a C-Apochromat water immersion objective (NA 1.2).

2.4.6 Cellular Permeability Measurements

Solutions of 2.5 μM sodium fluorescein (NaFL; Sigma-Aldrich) and 2.5 μM sulforhodamine 101 (SR101; Sigma-Aldrich) were prepared in phenol-free Ham's F-12 (Caisson Laboratories, Smithfield, UT). Gammagard Liquid Immune Globulin Intravenous (IgG; Lot # LE12L017AB; Baxter, Westlake Village, CA) was fluorescently labeled using an Alexa Fluor 647 Protein Labeling Kit (Life Technologies) according to the manufacturer's protocol. A solution of 10 mg/ml unlabeled IgG, spiked with 100 μg/ml of Alexa Fluor 647 labeled IgG, was prepared in phenol-free Ham's F-12. To begin the assay, the fluorescent solutions were added to monolayers pre-stained with CB. After transfer of the cells to a pre-heated microscopy stage, laser and gain settings for each fluorescent solution was adjusted such that the signal histogram covered the entire dynamic range of the detector. Next, z-stack ranges were set such that the datasets would encompass the glass coverslip, COL1 hydrogel, and the luminal fluorescent solution (see Figure 2-1A for reference). Using the 'time-series' function on the LSM Zen software, z-stack images were captured every 15 minutes for 1 hour. For consistency, z-stack images were captured at the center of the COL1 hydrogel. It is important to note that the imaging parameters should be optimized to minimize cellular photo-toxicity. Accordingly, z-stack images were captured with a low-resolution voxel size of $0.4251 \times 0.4251 \times 0.8100\ \mu m^3$ (x-y,

500 × 100 pixels) to enable a very short pixel dwell time of 0.87 microseconds. As the z-slices containing the cellular monolayer were approximately 3 or 4, there was a total cellular exposure time of 611 milliseconds, given the 152.77 millisecond scan time per frame. Once the time-lapse images were captured, they were processed in ImageJ. First, a z-stack image was 'resliced' to produce an equivalent dataset now showing the cross-section of the system (as illustrated in Figure 2-1A). Then, the resliced z-stack image was 'projected' with respect to average intensity. Subsequently, a box encompassing the entire hydrogel was drawn and the intensity within this region of interest was tabulated for each 15-minute time-point. Finally, the cellular permeability, P, was calculated using the equation

$$P = \frac{dI_{gel}}{dt}\frac{V}{A * I_{soln}}$$

where dI_{gel}/dt is the slope determined from the tabulated intensity versus time data, V is the volume of the gel, A is the lateral area of the gel (approximated as the chamber area), and I_{soln} is the intensity of the fluorescent solution above the cell monolayer. To calculate absolute molar values, RFU values were converted to concentration based on standard curves for each analyte, and multiplied by the hydrogel volume.

2.4.7 Photobleaching

A fluorescent solution of 2.5 μM NaFL, 100 μg/ml Alexa Fluor 647, and 10 mg/ml unlabeled IgG was prepared in phenol-free Ham's F-12. The solution was added to cells pre-incubated with CB, and subsequently placed in a pre-heated microscopy stage. Using the 'photobleaching' application in the Zeiss Zen software, cell-sized regions of interest were drawn and subsequently bleached using 100% laser intensity of a 488 nm argon laser. Regions were bleached until the affected cells lost

CB signal and appeared to round up, which indicated that the cells were no longer viable. Permeability of the photobleached monolayers was conducted as previous detailed.

2.4.8 NaFL and SR101 Accumulation Assay

A solution of 2.5 μM NaFL and 2.5 μM SR101 in phenol-free Ham's F-12 was added to cells pre-incubated with CB. After 15 minutes, the fluorescent NaFL and SR101 solution was replaced with fresh phenol-free Ham's F-12 and subsequently transferred to a pre-heated microscopy stage for imaging.

2.4.9 Statistical Analysis

GraphPad Prism v7.0c (GraphPad Software, La Jolla, CA) was used for statistical analysis. Unless specified otherwise, datasets were generated from four independent differentiations and evaluated for statistical significance using Student's t-test with $\alpha = 0.05$.

2.5 Results and Discussion

2.5.1 hiPSC-BMECs Form a Confluent Monolayer on COL1 Hydrogels

As the established hiPSC-to-BMEC differentiation process yields a mixed population of cells with neural and endothelial lineages, we tested whether COL1 hydrogels were able to selectively purify hiPSC-BMECs similar to coating matrices composed of fibronectin and collagen type IV (Lippmann et al. 2014). The COL1 hydrogel that forms the abluminal compartment of our BBB model (Figure 2-1A, left) was first optimized to support the formation of a confluent monolayer. To prevent infiltration of cells into the COL1 hydrogel during seeding, the COL1 concentration

and gelation temperature were selected to achieve an average mesh size less than 3 µm (Y. L. Yang, Leone, and Kaufman 2009). CRM analysis of 5 mg/ml COL1 hydrogels formed at 37 ºC showed an average mesh size of 1.03 ± 0.13 µm (Figure A-1). Differentiated hiPSCs subcultured on COL1 hydrogels formed a confluent monolayer with no viable cells present in the hydrogel, as assessed by CB cell viability staining (Figure 2-1A, right). To assess the expression and localization of relevant BMEC proteins, immunocytochemistry of hiPSC-derived cell monolayers formed on COL1 hydrogels was performed. Tight junction proteins occludin (OCLN) and claudin-5 (CLDN5) revealed continuous cell-cell contacts throughout the monolayer (Figure 2-1B). In addition, expression of transporters GLUT1 (glucose transporter 1) and MFSD2A (major facilitator superfamily domain-containing protein 2A) as well as PGP (efflux pump p-glycoprotein 1) localized on the cell membrane and showed uniform expression throughout the monolayer (Figure 2-1B).

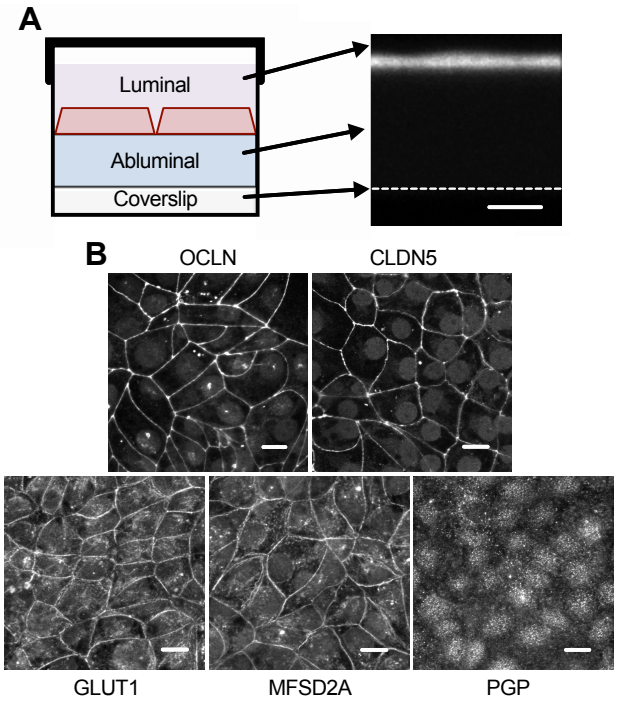

Figure 2-1: Characterization of hiPSC-BMECs subcultured on COL1 hydrogels. (A) An illustrative schematic of the COL1 hydrogel-based BBB model (left) and a representative cross-section of a z-stack confocal image probing for live-cell marker CB (white) (right). Scale bar is 10 µm. (B) Immunocytochemistry of hiPSC-BMECs on COL1 hydrogels examining for expression of tight junctions OCLN and CLDN5, transporters GLUT1 and MFSD2A, and efflux pump PGP. Scale bars are 10 µm.

The differentiated cells subcultured on COL1 hydrogels demonstrated the expression and proper localization of five BMEC-related proteins, including MFSD2A, a lipid transporter specific to endothelial cells of the central nervous system (Ben-Zvi et al. 2014). These cells were able to form a single, confluent monolayer on COL1 hydrogels, with no viable cells found within the hydrogel. These results confirm that COL1 hydrogels are able to selectively purify differentiated cells with a BBB-like phenotype and enable their formation of a confluent monolayer. Our ability to consistently form confluent monolayers without the addition of fibronectin, collagen type IV, or any extracellular matrix proteins may be attributed to the thin 30-50 µm thickness of the hydrogel that increases the stiffness experienced by cells as

opposed to much thicker hydrogels of equivalent characteristics (Ben-Zvi et al. 2014). The increased hydrogel stiffness can also explain the different results obtained in a recent report that demonstrates an inability to form confluent hiPSC-BMEC monolayers on a similar COL1 hydrogel with an average thickness of 300-500 µm (Katt et al. 2018). The importance of stiffness for hiPSC-BMEC monolayer formation is supported by their findings that increasing COL1 concentration, and subsequently stiffness, drastically increases monolayer coverage (Katt et al. 2018). Issues with monolayer confluence were attributed to the moving of or loss of the COL1 hydrogels on the glass surface. Conjugation of COL1 to EDC/NHS-activated glass addressed these issues and introduced no additional autofluorescence, similar to findings using EDC/NHS to crosslink COL1 hydrogels (Niu et al. 2016).

2.5.2 Quantifying large and small molecule permeability of hiPSC-BMECs on COL1 hydrogels.

In addition to the presence of relevant BMEC proteins, a BBB-like phenotype is confirmed by comparing the cellular permeability of benchmark molecules across a monolayer of cells to relevant reports. To quantify the permeability of molecules, we employed confocal microscopy to measure the transport of molecules from the luminal solution to the abluminal COL1 hydrogel. Here, NaFL (MW 376 Da) and IgG (MW 155 kDa) were selected as benchmark small and large molecules, respectively. Despite subtle differences in intensity profiles as a function of position within the hydrogel (Figure 2-2A), the molar flux of NaFL and IgG into the hydrogel was linear (Figure 2-2B). Accordingly, permeability values were calculated using an analogous equation established for insert-based BBB models, where a linear flux of the analyte into the abluminal compartment is a prerequisite (Siflinger-Birnboim et al. 1987). COL1

hydrogels in the absence of cells demonstrated a rapid, 10-second equilibration of NaFL or IgG with the luminal solution. Thus, permeability values of cell-free hydrogels were not measurable. Permeability of hiPSC-BMECs on 4 µL COL1 hydrogels were $3.70 \pm 0.37 \times 10^{-7}$ cm/s for NaFL and $2.69 \pm 0.90 \times 10^{-9}$ cm/s for IgG at day two of subculture (Day 2). Importantly, the measured NaFL or IgG permeability was not dependent on the hydrogel volume, as NaFL and IgG permeability values measured on 3 or 6 µL COL1 hydrogels (Figure A-2) were not significantly different than values obtained using 4 µL COL1 hydrogels.

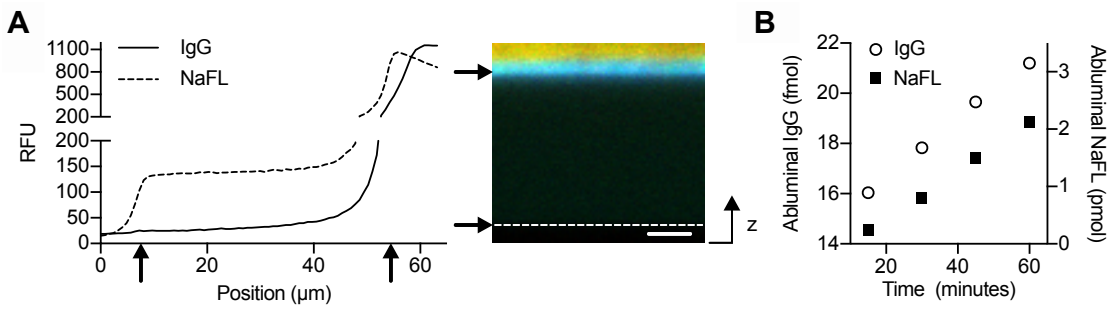

Figure 2-2: Confocal microscopy-based quantification of cellular permeability. (A) A representative relative fluorescence unit (RFU) profile of IgG and NaFL (left) along the luminal and abluminal compartments of a COL1-based BBB model, visualized as a z-stack confocal image (right). The merged signal of NaFL (green) and IgG (red) in the luminal compartment, above the hiPSC-BMEC monolayer positive for CB staining (blue), appears as yellow. The COL1 hydrogel abluminal compartment is denoted between the black arrows for both figures, and the white dashed line on the left figure represents the glass coverslip. Raw RFU values were normalized to the maximum luminal RFU measured for each respective analyte. Scale bar is 10 µm. (B) The corresponding, representative molar accumulation of IgG and NaFL within the COL1 hydrogel during a one-hour permeability assay.

The NaFL and IgG permeability values measured for the hiPSC-BMEC monolayer formed on COL1 hydrogels are comparable to values previously reported for hiPSC-BMECs grown on inserts (Mantle, Min, and Lee 2016; Lee et al. 2018; Canfield et al. 2017), and further supports the BBB-like phenotype observed at the protein expression level. Moreover, these results demonstrate that permeability values

can be quantified on COL1 hydrogels by measuring the abluminal molar flux of analytes via confocal microscopy and using a similar flux balance-derived permeability equation established for insert-based models. However, as with any fluorescence-based assay, the requirement of the analyte to be fluorescent is a central limitation in our model. Moreover, as fluorophores are often the same size as small molecules like caffeine, fluorescent conjugation could alter native transport across the BBB, and precautions should be taken to prevent misinterpretations of transport data. Previous reports using polyacrylamide hydrogels to characterize permeability normalized the abluminal analyte flux across a monolayer of cells relative to the abluminal analyte flux of cell-free hydrogels (Huynh et al. 2011). The similar flux between the cell-containing and cell-free conditions suggests that calculations of absolute permeability using polyacrylamide hydrogels must account for the cell-free hydrogel permeability in a similar manner to how blank insert permeability is accounted for in insert-based permeability calculations. In contrast, the high NaFL or IgG permeability of cell-free COL1 hydrogels suggests that the permeability of small and large analytes into the COL1 hydrogel is negligible in the measurement of cellular permeability. The difference in cell-free permeability is likely attributed to the nanometer-scale average mesh size of typical polyacrylamide hydrogels, which is three orders of magnitude smaller than our micrometer-scale average mesh size. The high cell-free permeability values and micrometer-scale average mesh size also imply a very fast diffusive timescale within our COL1 hydrogel, which are on the order of seconds for NaFL and IgG based on comparable measurements in a similar COL1 hydrogel (Kihara, Ito, and Miyake 2013). Thus, the timescale of permeability for NaFL and IgG, which range from approximately 10^{-7} to 10^{-9} cm/s, is several orders of

magnitude longer than that of diffusion, which was an important factor that enabled the quantification of permeability. Similarly, there are limitations in the values of permeability that can be measured with our model. In theory, permeability values up to 1×10^{-6} cm/s can be measured using a hydrogel volume of 6 μL and an interval time of 10 minutes. Although we demonstrate hydrogel volume does not alter the abluminal molar flux, and thus permeability, of NaFL and IgG, it does change the measured concentration in the abluminal compartment. Accordingly, hydrogel volume is an important consideration when using standard confocal microscopy to simultaneously measure the analyte signal in the luminal and abluminal compartments as signals from both compartments must fall within the dynamic range of the fluorescence detector. A hydrogel volume of 4 μL was sufficient to obtain abluminal NaFL and IgG signals above background while maintaining corresponding luminal signals below detector saturation. Accordingly, all subsequent experiments were performed using a 4 μL COL1 hydrogel.

2.5.3 hiPSC-BMECs on COL1 Hydrogels Exhibit an Increase in Cellular Permeability Over Multiple Days

The ability of BMEC monocultures to maintain or decrease barrier integrity is an important factor to consider in multi-day assays. Accordingly, NaFL and IgG permeability of hiPSC-BMEC monolayers on COL1 hydrogels was measured multiple days post-subculture. To determine whether hiPSC-BMEC monolayers on COL1 hydrogels maintain the low permeability of NaFL and IgG observed at Day 2, NaFL and IgG permeability was measured daily from Day 2 to Day 5. Daily permeability measurements were normalized to average Day 2 values and subsequently compared for changes. Normalized permeability of NaFL and IgG from Day 3 to Day 5 was

significantly higher than Day 2 values (Figure 2-3). Moreover, the normalized permeability increased linearly from Day 2 to Day 5 for both NaFL and IgG (Figure 2-3). However, the daily rate of increase of 1.52 ± 0.29 for IgG was significantly higher than that of 0.66 ± 0.05 for NaFL ($p = 0.0257$). Permeability values past Day 5 were not measured as some monolayers had observable CB-negative cell-sized holes and were no longer confluent. To address whether the daily increase in permeability from Day 2 to Day 5 was attributed to the presence of one or more undetected defects in the cell monolayer, one or two cells in Day 2 hiPSC-BMECs were compromised through photobleaching and NaFL and IgG permeability was subsequently measured. A rounded morphology and loss of cell viability marker CB confirm that photobleaching produced compromised cells, which appeared as CB-negative spaces in the monolayer (Figure A-3A). There was no significant difference in NaFL or IgG permeability between Day 2 monolayers with one or two compromised cells (Figure A-3B). The IgG permeability of Day 2 monolayers with one compromised cell was significantly higher than that observed for intact monolayers from Day 2 to Day 5 ($p = 0.0123$). However, only Day 2 and Day 3 ($p = 0.0201$) NaFL permeability values were significantly lower than compromised Day 2 values with one compromised cell.

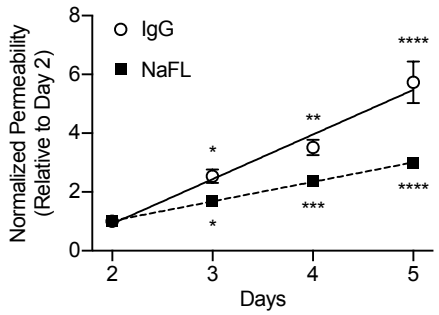

Figure 2-3: Normalized NaFL and IgG permeability of hiPSC-BMECs on COL1 hydrogels as a function of day(s) post-subculture. NaFL and IgG permeability values were normalized to corresponding Day 2 values. Linear regressions of IgG (solid) and NaFL (dashed) had R^2 values of 0.977 and 0.999, respectively. Day 2 values were compared to Day 3-5 values using one-way ANOVA followed by Dunnett's multiple comparison test (*$p < .05$, **$p < 0.01$, ***$p < 0.001$, ****$p < 0.0001$). Values are mean ± SEM of four independent differentiations. Each set of differentiated cells was seeded in four individual hydrogels, and daily permeability value measurements were conducted on unanalyzed hydrogels.

The increasing NaFL and IgG permeability values of hiPSC-BMEC monolayers on COL1 hydrogels were similar to previous reports showing decreasing TEER over multiple days for hiPSC-BMECs grown on porous inserts (Mantle, Min, and Lee 2016; Qian et al. 2017; Lippmann et al. 2014), further supporting that hiPSC-BMECs exhibit similar characteristics on both COL1 hydrogels or porous inserts (Katt et al. 2018). Loss of barrier function of cultured hiPSC-BMECs over time is suspected to be associated with the lack of induction by cells that naturally support the BBB (astrocytes, pericytes and neurons). Indeed, when hiPSC-BMECs are co-cultured with these BBB-supportive cells, barrier function is enhanced and maintained for a longer duration than hiPSC-BMECs grown in monoculture (Canfield et al. 2017). The normalization of permeability values relative to Day 2 values allowed for a scaled comparison between daily increases in NaFL and IgG permeability. The nearly two-fold higher daily rate of normalized permeability increase for IgG relative to NaFL suggests that large molecule transport is especially sensitive to the changes in

transcellular and paracellular transport routes that occur in extended culture of hiPSC-BMECs. Although there are no previous reports examining alterations in transport pathways of BMECs, these results support the common practice of assaying hiPSC-BMECs at two days after subculture and suggest careful interpretation of data when using these cells in multi-day assays. The decrease in barrier function was not attributed to the emergence of defects within the hiPSC-BMEC monolayer, as IgG permeability at Day 5 was significantly lower than that observed for compromised Day 2 monolayers with a single compromised cell. However, NaFL permeability of uncompromised Day 4 and Day 5 monolayers were not significantly different than compromised Day 2 monolayers, which suggests that by Day 4 the hiPSC-BMECs may have drastically lost their ability to restrict the transport of small molecules. These observations agree with the sharp increase in ion permeability, or conversely a decrease in TEER, that often occurs after Day 3 of subculture (Mantle, Min, and Lee 2016; Qian et al. 2017). Finally, the large, significant differences in cellular permeability between uncompromised monolayers and those with even one compromised cell highlights the sensitivity of the confocal-based quantification system to detect the impact of a non-confluent hiPSC-BMEC monolayer on cellular permeability.

2.5.4 Small Molecules NaFL and SR101 Display Different Intracellular Processing and Cellular Permeability

The transport of molecules by efflux pumps is an important characteristic of in vitro BBB models. To study how two substrates of efflux pump MRP1, NaFL and SR101, are processed by hiPSC-BMECs, we used confocal microscopy to characterize their intracellular distributions and cellular permeability. Utilizing live-cell probe CB

as a reference for the location of the hiPSC-BMEC monolayer, we observed accumulation of NaFL, but not SR101, within the cells after 15 minutes with NaFL and SR101 in the luminal compartment (Figure 2-4A). Moreover, the intracellular NaFL signal (12-15 μm) was higher than abluminal or luminal signals (Figure 2-4A). Next, NaFL and SR101 were removed from the luminal compartment to better enable intracellular visualization within the hiPSC-BMECs. NaFL was observed throughout the cell but mainly localized within the cytosol, where colocalization with CB was the strongest (Figure 2-4B). SR101 was found within vesicular structures, where NaFL and CB staining was absent (Figure 2-4B). To assess whether intracellular accumulation can affect cellular permeability, the permeability of NaFL and SR101 across hiPSC-BMECs was compared. The permeability of SR101 was $4.81 \pm 0.47 \times 10\text{-}8$ cm/s, which was significantly lower than NaFL permeability ($p = 0.0002$).

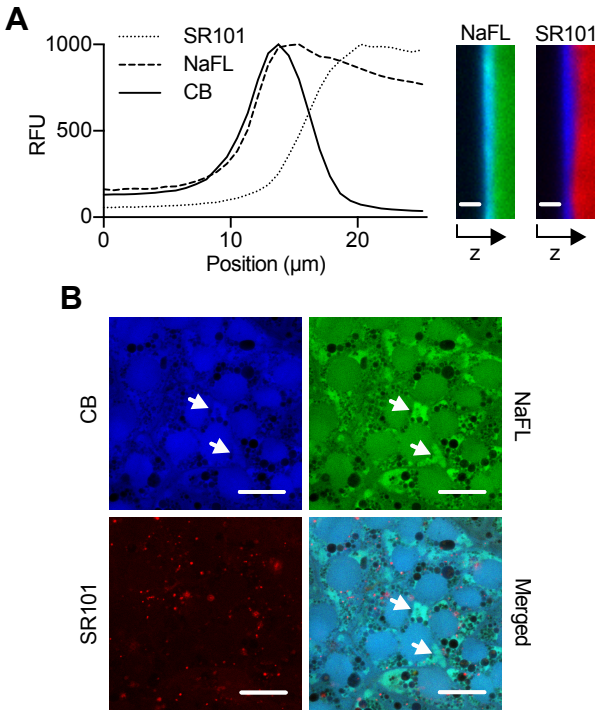

Figure 2-4: Localization of MRP1 substrates within hiPSC-BMECs using confocal microscopy. (A) A representative relative fluorescence unit (RFU) profile of SR101, NaFL, and CB (left) from the abluminal to luminal compartment of a COL1-based BBB model. A cross-section of the corresponding z-stack confocal image that has been split to demonstrate the accumulation of NaFL (green) or SR101 (red) within the hiPSC-BMEC monolayer positive for CB live-cell staining (blue). The images span the abluminal and luminal compartments. RFU values were normalized to the maximum RFU observed for each probe. Scale bar is 10 µm. (B) Individual and merged confocal images showing CB, NaFL, and SR101 localization within a hiPSC-BMEC monolayer following 15 minute treatment with 2.5 µM NaFL and SR101. Arrows highlight the colocalization of CB and NaFL within the cytosol. Scale bar is 20 µm.

Efflux pump activity is a key attribute of the BBB and leads to the restriction of many small molecule drugs (Pardridge 2012). A thorough characterization of how known efflux pump substrates are processed by the BBB in vitro could aid the development of descriptors that predict BBB efflux activity of new drug candidates. Although a comparison of net influx and efflux for known efflux pump substrates is often characterized for hiPSC-BMECs, such as the polarization of rhodamine 123

(Qian et al. 2017; Mantle, Min, and Lee 2016; Lippmann et al. 2014), a description of intracellular localization of efflux pump substrates is lacking. Accordingly, we characterized the intracellular distributions and cellular permeability of NaFL and SR101, which are both substrates of the efflux pump MRP1 (Kaufmann, Toro-Ramos, and Krise 2008; Sun, Miller, and Elmquist 2001) present at the BBB and in hiPSC-BMECs (Qian et al. 2017). We observed that NaFL accumulated within hiPSC-BMECs, and localized predominately within the cytosol. Our results are in agreement with findings showing NaFL internalization within primary bovine BMECs in vitro (Sun, Miller, and Elmquist 2001) and in the rat BBB in vivo (Sun, Miller, and Elmquist 2001; Hawkins et al. 2007). Additionally, we observed that NaFL reached intracellular concentrations higher than those observed in the luminal compartment, which suggests that the internalization is not passive. Indeed, an in vivo rat study demonstrated that NaFL is also a substrate of organic anion transporter-3 (OAT3) at the BBB (Hawkins et al. 2007), and suggests that active transcellular transport of NaFL is likely. Unlike NaFL, SR101 did not accumulate within the cytosol, but was found within vesicular structures of hiPSC-BMECs. Although there are no previous reports investigating SR101 localization within BMECs, the presence of SR101 within vesicular structures has been reported for other cell types, which was shown to occur via dynamin- and clathrin-dependent endocytosis (Wen, Saltzgaber, and Thoreson 2017). Moreover, the cytosolic exclusion of SR101 by hiPSC-BMECs is in agreement with studies demonstrating MRP1-dependent exclusion of SR101 using HeLa cells (Kaufmann, Toro-Ramos, and Krise 2008). Interestingly, despite the nearly two-fold higher molecular weight of SR101 (MW 607) relative to NaFL, we found that SR101 permeability was nearly an order of magnitude lower than NaFL permeability. The

significantly lower permeability of SR101 relative to NaFL suggests that although tight junctions restrict the paracellular transport of NaFL and SR101, the intracellular accumulation observed for NaFL may lead to its increased transport across hiPSC-BMECs. This interpretation is supported by a previous report from our group demonstrating that NaFL permeability maintains low permeability (approximately 3 × 10-7 cm/s) while TEER, an established metric of passive transport, continues to increase (Mantle, Min, and Lee 2016). However, additional studies will be needed to elucidate the roles of MRP1 and OAT3 in regulating the differential transport and intracellular compartmentalization of NaFL and SR101. Overall, these results suggest that transporter and efflux pump function should be considered when interpreting transport data, and that the direct visualization of intracellular processes can aid these interpretations.

2.6 Conclusions

Currently, the majority of studies using *in vitro* BBB models rely on insert-based experimental systems to characterize the permeability of potential therapeutic drugs, which can help make meaningful predictions of their transport across the BBB *in vivo* (Mantle, Min, and Lee 2016). However, these insert-based BBB models do not enable complementary studies to visualize dynamic, intracellular processes that help elucidate cellular mechanisms regulating transport. Knowledge of newly characterized transport mechanisms has enabled the development of potential strategies to improve therapeutic drug delivery across the BBB (Weber et al. 2018; Villaseñor et al. 2017). Accordingly, an *in vitro* BBB model that enables the characterization of both permeability and intracellular dynamics of therapeutic drugs can help integrate findings from independent permeability and intracellular processing studies. Here, we

presented an *in vitro* two-dimensional COL1-based BBB model that is facile to construct and, to our knowledge, is the first to report the simultaneous visualization of dynamic intracellular processes and quantification of cellular permeability using confocal microscopy. The ability of hiPSC-BMECs, which have previously been shown by our group to be an excellent human model of the BBB (Mantle, Min, and Lee 2016), to exhibit a BBB-like phenotype on COL1 hydrogels similar to that observed for inserts illustrates that findings using the two different experimental systems are translatable. Finally, the differences in cellular permeability and intracellular processing observed for two representative small molecule substrates of efflux pump MRP1 highlight the importance of thoroughly characterizing transport to make meaningful connections between permeability and processing of therapeutic drugs at the BBB.

Chapter 3

ANTIBODY TRANSCYTOSIS ACROSS BRAIN ENDOTHELIAL-LIKE CELLS OCCURS NONSPECIFICALLY AND INDEPENDENT OF FcRn

3.1 Preface

This chapter is adapted from: Ruano-Salguero JS and Lee KH. (2020) Antibody transcytosis across brain endothelial-like cells occurs nonspecifically and independent of FcRn, with permission (see Appendix D).

This chapter builds on the COL1-based BBB model and transport quantification established in Chapter 2 and addresses the influence of FcRn on IgG transport. A fluorescence microscopy-based method to quantify intracellular accumulation of endocytosed IgG was developed to confirm the FcRn-mediated recycling of a native IgG and the lack of recycling for an IgG unrecognized by FcRn. Subsequent concentration and inhibitory studies with recognized or unrecognized IgG were performed to identify possible influences of FcRn on IgG transport. IgG fragments, RMT ligands, and large/small dextrans indicated were used for comparisons and were coupled with biophysical characterizations to confirm the transport pathway employed by each macromolecule.

The authors thank Dr. Jeff L. Caplan at the Delaware Biotechnology Institute's Bioimaging Center (University of Delaware) for assistance with super-resolution Airyscan confocal microscopy and object-based segmentation in Volocity, and Angela M. Norton at the University of Delaware for helpful discussions. This work was funded in part by a NSF GRFP fellowship (Award Number 1247394). Microscopy

access was supported by grants from the NIH (NIGMS – P20 GM103446; 1 S10 OD016361), the NSF (IIA-1301765) and the State of Delaware.

3.2 Abstract

The blood-brain barrier (BBB) hinders the brain delivery of therapeutic immunoglobulin γ (IgG) antibodies. Evidence suggests that IgG-specific processing occurs within the endothelium of the BBB, but any influence on transcytosis remains unclear. Here, involvement of the neonatal Fc receptor (FcRn), which mediates IgG recycling and transcytosis in peripheral endothelium, was investigated by evaluating the transcytosis of IgGs with native or reduced FcRn engagement across human induced pluripotent stem cell-derived brain endothelial-like cells. Despite differential trafficking, the permeability of all tested IgGs were comparable and remained constant irrespective of concentration or competition with excess IgG, suggesting IgG transcytosis occurs nonspecifically and originates from fluid-phase endocytosis. Comparison with the receptor-enhanced permeability of transferrin indicates that the phenomena observed for IgG is ubiquitous for most macromolecules. However, increased permeability was observed for macromolecules with biophysical properties known to engage alternative endocytosis mechanisms, highlighting the importance of biophysical characterizations in assessing transcytosis mechanisms.

3.3 Introduction

The brain endothelial cells (BECs) that form the main structural component of the blood-brain barrier (BBB) are central to the protection of brain parenchyma. Unique from peripheral endothelium, BECs exhibit substantially reduced permeability of most bloodborne molecules (Zhao et al. 2015). Accordingly, this restrictive

physiology also poses a formidable obstacle in the brain delivery of therapeutic molecules (Pardridge 2012). In particular, conventional immunoglobulin γ (IgG) antibody-based passive immunotherapies, which are structurally and functionally similar to endogenous IgGs, only demonstrate brain uptake of 0.1–0.3% of the injected dose (Sevigny et al. 2016; Wang et al. 2018). Despite the need to improve the brain delivery of conventional therapeutic IgGs (Golde 2014), progress is hindered by the current lack of understanding regarding their interactions with BECs.

IgG-endothelium interactions in the periphery are dominated by the neonatal fragment crystallizable (Fc) receptor (FcRn). Following internalization of circulating IgG, the acidic microenvironment of endosomal compartments enables FcRn to bind and recycle IgG back to the lumen in a pH-dependent manner (Ward and Ober 2018). FcRn-mediated recycling therefore limits lysosomal degradation and contributes to the extended serum half-life of IgGs. However, FcRn can also mediate the abluminal transcytosis of IgG, which is exemplified in the transfer of maternal IgG across the placental endothelium. In this regard, FcRn is a unique transcytosis receptor, e.g. compared to the transferrin receptor (TfR) (Goulatis and Shusta 2017), as it can shuttle its ligand bidirectionally to either cell surface (i.e. luminal recycling or abluminal transcytosis) (Pyzik et al. 2019). Traditional transcytosis (RMT) pathways are categorized as fluid-phase (e.g. macropinocytosis) or adsorptive-mediated, which occur via specific (e.g. receptor-mediated transcytosis (RMT)) or nonspecific (e.g. electrostatic adsorption) processes. The mechanisms regulating the preference for luminal or abluminal shuttling by FcRn remain to be determined, but are likely tissue and organ-specific (Ward and Ober 2018; Pyzik et al. 2019; Kuo and Aveson 2011). Accordingly, FcRn functionality in BECs may not mirror those reported for other

endo- or epithelium (e.g. intestinal) in which IgG transcytosis is observed (Pyzik et al. 2019).

Since the initial detection of FcRn in BECs over 15 years ago (Schlachetzki, Zhu, and Pardridge 2002), its role in mediating recycling or transcytosis of IgG across BECs has remained uncertain. First, no study has yet confirmed the recycling of IgG by BECs *in vivo* or *in vitro*. Indirect evidence of potential FcRn-mediated recycling was provided by a recent *ex vivo* study demonstrating the partial localization of endogenous mouse IgGs within BECs to lysosomal compartments (Villasenõr et al. 2016). These findings have led to speculation whether lysosomal degradation is a contributing factor to the limited BBB permeability of IgG, but this hypothesis remains unconfirmed (Villasenõr et al. 2016). Second, there is no consensus on the role of FcRn in influencing the blood-to-brain transcytosis of IgG across BECs despite several notable studies (Deane et al. 2005; Cooper et al. 2013; Banks et al. 2002; Abuqayyas and Balthasar 2013; Chen et al. 2014; Yip et al. 2014). The use of cross-species systems, e.g. human IgG in mice, has been identified as a potential confounding factor (St-Amour et al. 2013), given the importance of binding affinity in proper FcRn-IgG engagement (Ward et al. 2003; Ober et al. 2001). Similarly, FcRn knockout models may also generate confounding results as there is the potential to engage compensatory mechanisms that could mask the effect of FcRn deletion (Garg and Balthasar 2009). Alternative inhibitory and comparative studies, such as using excess levels of IgG or comparing IgGs with native or reduced FcRn binding (Yip et al. 2014), have been identified as a more direct approach over FcRn knockout models (Garg and Balthasar 2009). These alternative IgG-based approaches can also investigate the potential role of other IgG-specific receptors in mediating IgG

transcytosis across BECs, which may be commensurate with FcRn (Deane et al. 2005).

An additional variable that may contribute to the conflicting findings is the influence of IgG concentration on the observed transcytosis pathway employed by BECs. Consistent with receptor-mediated processing, IgG transcytosis across BECs has been reported as being concentration dependent (St-Amour et al. 2013; Zlokovic et al. 1990). However, several reports observe no evidence of concentration-dependent phenomena (Sevigny et al. 2016; Wang et al. 2018; Atwal et al. 2011). A potential confounding factor between such findings is the presence or absence of endogenous IgG, which is influenced by the particular experimental method (e.g. *in situ* brain perfusion). The presence of endogenous IgGs could mask the influence of IgG-specific receptors on transcytosis, and result in concentration-independent observations. Accordingly, the decreasing serum concentration of exogenous IgG, which is exacerbated in FcRn knockout models or when the IgG lacks FcRn binding, and the presence of endogenous IgG represent experimental hurdles to the assessment of IgG transcytosis across BECs *in vivo*.

Here we investigated the role of FcRn or other IgG-specific receptors in influencing the transcytosis of IgG across BECs *in vitro* using BEC-like cells derived from human induced pluripotent stem cells (iBECs). We have previously shown that iBECs exhibit permeability of IgG that is more restrictive than that observed for the rat BBB *in vivo* (Shi et al. 2014; Ruano-Salguero and Lee 2018; Mantle, Min, and Lee 2016), which supports its use as a representative BBB model. To compare the influence of FcRn engagement we assessed the intracellular processing and transcytosis of IgGs lacking human FcRn recognition, and we used human IgG as a

control, at varying concentrations and in the presence of excess human IgG. Our findings are consistent with FcRn as a key regulator of IgG recycling in BECs, help clarify the transcytosis mechanism influencing the limited BEC permeability of IgG, and exemplify the need to characterize biophysical attributes of macromolecules to meaningfully interpret BEC permeability.

3.4 Methods

3.4.1 Hydrogel-Based *In Vitro* BBB Model

COL1 from rat tendon (Corning) was prepared as a hydrogel on 8-chambered glass coverslips based on methods previously described (Ruano-Salguero and Lee 2018). IMR90-4 (WiCell) human induced pluripotent stem cells were maintained and differentiated to BECs as previously described (Mantle, Min, and Lee 2016; Ruano-Salguero and Lee 2018; Lippmann et al. 2014). After 8 days of differentiation, cells were dissociated with STEMPRO Accutase (Life Technologies) and suspended as single-cells. Cells were then added to preassembled hydrogels at a density of at least 1 million cells/cm^2. The cells were allowed to form a confluent monolayer by replacing the medium, which consisting of 0.1% human serum from platelet poor plasma (MilliporeSigma) in human endothelial SFM (Life Technologies), for the next two subsequent days. Construction of the hydrogel-based BBB model is illustrated in the supplement (Figure B-1a). All experiments were performed on the second day after subculture.

3.4.2 Quantitative Reverse Transcription Polymerase Chain Reaction

Confluent monolayers of iBECs were dissociated with STEMPRO Accutase and pelletized. Total RNA was isolated from the cell pellet using the RNeasy Micro

Kit (Qiagen). qRT-PCR was performed with the TaqMan RNA-to-Ct 1-Step Kit (Applied Biosystems) using commercial primer/probe sets (Integrated DNA Technologies). The total RNA from three independent differentiations was used for qRT-PCR analysis and run in technical triplicate.

3.4.3 Western Analysis of FcRn

Frozen, pelletized iBECs were lysed with radioimmunoprecipitation assay (RIPA) buffer at 0.5 million cells/mL and boiled at 95 ºC for 10 mins in sodium dodecyl sulfate (SDS) loading buffer (New England BioLabs) containing dithiothreitol. Biotinylated human FcRn (ACRO Biosystems) was loaded at 0.5 µg per lane and used as a positive control. Gel electrophoresis was performed in precast 4-20% Mini PROTEAN TGX gels (Bio-Rad), and the proteins were then transferred to Immobilon-P membranes (EMD Millipore). The membrane was blocked with 3% non-fat dry milk in Tris-buffered saline with TWEEN-20 (3%-TBST, Sigma) and then probed overnight at 4ºC with 2 µg/mL anti-human FcRn antibody in 3%-TBST (sc-66892, Santa Cruz Biotechnology). The membrane was then probed with alkaline phosphatase-conjugated goat anti-rabbit antibody at a 1:5000 dilution (Sigma) for 1 hour at 4 ºC. Signals were detected with an enhanced chemifluorescence substrate (GE Healthcare Life Sciences) and imaged using a Typhoon FLA-7000 scanner (GE Healthcare Life Sciences).

3.4.4 Fluorophore-IgG Conjugation and Deglycosylation

Pooled human IgG (Gammagard) and the four human IgG subclasses (MilliporeSigma) were dialyzed in PBS to remove glycine in the storage formulation. Mouse, rat, and rabbit IgGs (MilliporeSigma) were obtained as a powder and

reconstituted in PBS. Fluorescent labeling of IgG was performed using a 2 mg-scale Alexa Fluor 647 Protein Labeling Kit (Invitrogen) according to the manufacturer's protocol. Fluorescently-labeled IgG1 was deglycosylated using a 0.5 mg-scale GlycINATOR spin column (Genovis) according to the manufacturer's protocol. All labeled IgGs were concentrated using a spin column with a MW cutoff of 2.5 kDa to achieve a concentration above 5 g/L.

3.4.5 Pulse-Chase Assay and Immunocytochemistry

After iBECs were pulsed with Alexa Fluor 647-labeled IgG (human or mouse, 667 nM) or human transferrin (66.7 and 667 nM, Jackson ImmunoResearch) diluted in Phenol-free Ham's F-12 (Caisson) for 1 hour, the fluorogenic solutions were replaced with Phenol-free Ham's F-12. Immediately after, 16% (v/v) paraformaldehyde (Electron Microscopy Sciences) was added to the medium for a final concentration of 4% (v/v). Following 30 minutes of fixation, cells were extensively rinsed with PBS. Cells were then permeabilized with 0.1% (v/v) Triton X-100 (MilliporeSigma) for 5 minutes, treated with 3 µg/mL mouse anti-LAMP2 antibody (Invitrogen) overnight at 4 ºC, and then extensively rinsed with PBS. For detection, the cells were then treated with 5 µg/mL Alexa Fluor 488-labeled rabbit anti-mouse IgG (Invitrogen) for 1 hour at room temperature. Nuclei were labeled with NucBlue (DAPI; Life Technologies) as recommended by the manufacturer.

3.4.6 Super-Resolution Airyscan Confocal Microscopy

Fixed samples were imaged with a Zeiss 880 confocal microscope equipped with an Airyscan detector and a C-Apochromat 40× water immersion objective (NA 1.2) (Zeiss). Images with a voxel size of 0.0497 × 0.0497 × 0.083 μm^3 (x-y-z, 3876 ×

3876 × 1 pixel) were captured using the Airyscan Super-Resolution mode in Zen Black (Zeiss) and an appropriate filter cube. An optimal laser and gain setting was determined for each sample (e.g. 66.7 nM human transferrin), and was not changed when imaging biological replicates. The same imaging parameters were used to generate standard curves for images obtained from each serially diluted inoculum solution. Accordingly, all corresponding images for each sample, including the standard solution images, were batch processed in Zen Black using the same deconvolution parameters.

3.4.7 Quantitative Image Processing and Analysis

Object-based statistics and 3D object-based colocalization was performed in Volocity (Perkin Elmer). First, objects were detected using the 'Find Object' function for each z-stack image. Threshold intensity values were set as 3 standard deviations from the mean for each image. Large overlapping objects were segmented using the 'Separate Touching Object' function with a suggest volume size of 0.5 μm^3. Objects with a volume less than 0.05 μm^3 were excluded from all analysis as they were below the resolution of the images. For colocalization analysis, the 'Calculate Object Colocalization' function was used to measure the Manders M1 and M2 overlap coefficient between the Alexa Fluor 488 (LAMP2) channel and the Alexa Fluor 647 (macromolecule) channel. Colocalized objects with less than 30% overlap (M1 or M2 < 0.3) were not considered colocalization events in our analysis. Colocalization is represented as the percentage of vesicles that colocalized with LAMP2 relative to the total number of vesicles.

3.4.8 Live-Cell Permeability Assay

After medium replacement on the second day post-subculture, solutions containing fluorescent macromolecules and internal control were prepared. Unless noted otherwise, medium was replaced with 667 nM of fluorescently-labeled macromolecules in Phenol-free Ham's F-12. As an internal control, each solution also contained 2 μM sodium fluorescein, except for 155-kDa dextran which used a Alexa Fluor 647-labeled human IgG as an internal control. Datasets with internal controls that exhibited permeability values 2-fold higher than that previously reported were not analyzed because they were indicative of a non-confluent iBEC monolayer (Ruano-Salguero and Lee 2018). After aspiration of the culture medium, the analyte-containing solutions were added to each chamber of the 8-chambered glass coverslip. The vessels were then immediately mounted in a preheated stage within a humidified enclosure at 37 ºC and 5% CO_2. Imaging was performed with a Zeiss 710 confocal microscope with a C-Apochromat 40× water immersion objective (NA 1.2). Time-lapse z-stacks that contained both the luminal and abluminal (hydrogel) compartments were captured every 15 minutes using image acquisition parameters previously described (Ruano-Salguero and Lee 2018). Briefly, time-lapse z-stacks were processed in ImageJ as previously described and the average intensity of the fluorescent analyte within the hydrogel was measured at each time point (Ruano-Salguero and Lee 2018). The apparent cellular permeability, P_{app}, was calculated using the equation

$$P_{app} = \frac{V}{A \bullet I_{solution}} \frac{dI_{hydrogel}}{dt}$$

where V is the volume of the hydrogel, A is the lateral area of the chamber area, $I_{solution}$ is the intensity of the luminal solution and $dI_{hydrogel}/dt$ is the slope determined from the intensity versus time data measured via ImageJ An illustration of the permeability measurement procedure is provided in the supplement (Figure B-1b).

The 10-kDa dextran (labeled with Texas Red) was purchased from Invitrogen (D1828), the 155-kDa dextran (labeled with tetramethylrhodamine) was purchased from MilliporeSigma (T1287), and the anti-green fluorescent protein sdAb (labeled with ATTO 647N) was purchased from Chromotek. Human Fab and Fc (labeled with Alexa Fluor 647) was purchased from Jackson ImmunoResearch Laboratories.

3.4.9 Isoelectric Focusing

Polyacrylamide gel-based 1D IEF was performed using a pH 3–10 Criterion IEF Precast Gel (Bio-Rad). Samples were loaded at approximately 2 µg, and the 4.45–9.6 pI standard (Bio-RaD) was diluted 5-fold. The gel was run in a Criterion cell (Bio-Rad) according to the manufacturer's protocol. Afterwards, the pI standard was visualized with SYPRO Ruby (Invitrogen) using the 'Rapid' protocol provided by the manufacturer.

3.4.10 Statistical Analysis

GraphPad Prism 7 was used for statistical analysis. Comparison of data was performed using Student's t-test, and one-way and two-way ANOVA with $\alpha = 0.05$. All experiments were carried out with at least three biological replicates, where a unique differentiation (derived from an independent passage) constitutes one biological replicate, to determine statistical significance. The selection of appropriate statistical test and exact sample size is indicated in each figure legend.

3.5 Results

3.5.1 FcRn Mediates IgG Recycling in iBECs and Reduces Lysosomal Accumulation

To evaluate whether iBECs exhibit FcRn-mediated IgG recycling, we compared the intracellular processing of human IgG with that of mouse IgG, which lacks human FcRn recognition (Ober et al. 2001). Initially we confirmed the expression of FcRn in iBECs via quantitative reverse transcription polymerase chain reaction (qRT-PCR) (Figure B-2) and western analysis (Figure B-3). Using high sensitivity super-resolution Airyscan confocal microscopy, intracellular visualization revealed no significant differences in the average size or number of vesicular structures that contained fluorescently-labeled mouse or human IgG after a one-hour pulse (Figure 3-1a,b, and Figure B-4). Immunocytochemistry of lysosomal-associated membrane protein 2 (LAMP2), a lysosomal marker, was performed because of the possibility of differences in lysosomal shuttling (Figure B-5). Subsequent 3D object-based colocalization analysis revealed that over ~80% of mouse or human IgG-containing structures were LAMP2-positive lysosomes (Figure 3-1c). LAMP2 colocalization analysis also revealed that there was no significant difference in their extent of lysosomal compartmentalization (Figure 3-1c). Thus we hypothesized that although IgGs are eventually shuttled to any available lysosome, FcRn-mediated recycling of human IgG would lead to a lower extent of intracellular accumulation relative to mouse IgG. To quantify accumulation, the average vesicle intensity for each IgG was normalized by its corresponding inoculum solution intensity. Consistent with preferential recycling of human IgG by human FcRn, the normalized accumulation of human IgG was nearly 11-fold lower than that of mouse IgG (Figure 3-1d).

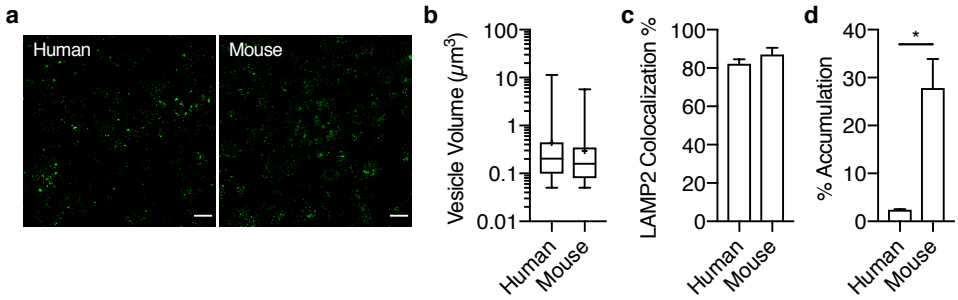

Figure 3-1: Lysosomal sorting of IgG is independent of FcRn-mediated salvaging in iBECs**.** (**a**) Representative deconvolved Airyscan super-resolution confocal images showing the intracellular vesicular structures containing fluorescently-labeled (i) human or (ii) mouse IgG (green) in fixed iBECs after a 1-hr pulse with 667 nM of either IgG. Images are Z-projections based on average intensity, and scale bar represents 20 µm. (**b**) Representative vesicle diameter distribution of IgG-containing structures. Distributions are from one 192 × 192 μm^2 image for each IgG, and are shown as boxplots with interquartile ranges and median. The mean is shown as a cross and error bars represent minimum and maximum values. (**c**) Quantification of colocalization between LAMP2 and either IgG using 3D object-based analysis. (**d**) Quantification of average vesicle intensity for either IgG relative to its inoculum intensity. Values in (c) and (d) represent means from three independent differentiations ± SEM, where each value is an average from five 192 × 192 μm^2 images. Means were compared using two-tailed Student's t-test (*$P < 0.05$).

3.5.2 IgG Transcytosis Across iBECs is not Receptor-Mediated

Given that FcRn was actively recycling human IgG, we evaluated whether FcRn was also mediating its transcytosis. To ensure the same intracellular phenomena were reproduced, the permeability of IgG was measured within the same one-hour timeframe and concentration previously used. Using live-cell microscopy-based permeability quantification, no significant differences between mouse and human IgG were observed (Figure 3-2a). Similar permeability values were also observed for rat and rabbit IgG (Figure 3-2a), which are comparable to mouse and human IgG with respect to human FcRn binding (Ober et al. 2001), respectively. IgG from mice, rabbits, and rats also exhibit differences throughout the Fc domain that are distinct

from the FcRn binding motif. It is therefore possible that these differences could engage other Fc-specific processes that alter their transcytosis by FcRn. Accordingly, the four human IgG subclasses (IgG1–4) were assessed separately as their Fc domains are conserved but only IgG3 exhibits a mutation on the FcRn binding motif (Ward et al. 2003). Also, because glycosylation has been speculated to alter BEC permeability (Finke et al. 2017), an aglycosylated IgG1 was assessed. Consistent with the initial observations, there was no significant difference in permeability between the four human IgG subclasses, or between glycosylated and aglycosylated IgG1 (Figure 3-2b). Finally, any influence imparted by the Fc domain on IgG transcytosis was evaluated by comparing the permeability of the Fc with that of the antigen-binding fragment (Fab). In contrast with Fc-dependent transcytosis, the permeability between the two IgG fragments was not significantly different (Figure 3-2c). Therefore these findings suggest the possibility that FcRn, or any other potential Fc receptor, do not directly mediate IgG transcytosis across iBECs.

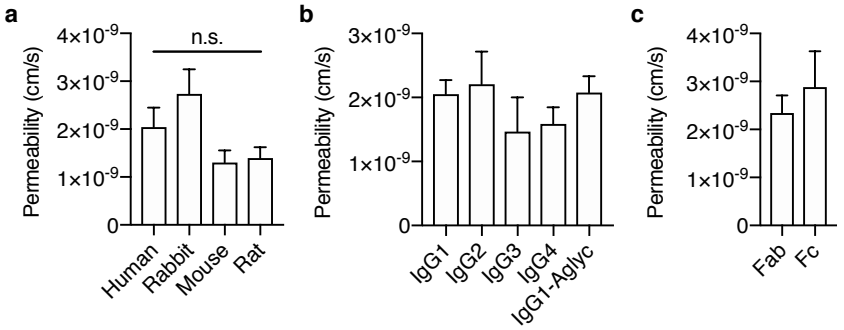

Figure 3-2: FcRn engagement does not alter iBEC permeability of IgG or its fragments. (a) The permeability of various serum-derived polyclonal IgGs of human, rabbit, mouse, and rat origin. (b) The permeability of the four human IgG subclasses, and an aglycosylated variant (IgG1-Aglyc). (c) The permeability of human IgG fragments, Fab and Fc. Molar concentration for all IgGs and fragments was 667 nM. Values are the mean of four (a and b) or three (c) independent differentiations ± SEM, and were compared using one-way ANOVA followed by Tukey's multiple comparison test (n.s., $P > 0.05$) (a and b) or two-tailed Student's t-test (c).

3.5.3 iBECs Exhibit Non-Saturable Transcytosis of IgG

We next investigated whether the intracellular trafficking of IgG indirectly influenced its transcytosis. Processes tangential to transcytosis, such as FcRn-mediated recycling or lysosomal shuttling (Villasenõr et al. 2016), may divert the intracellular flux of IgG and lead to a decrease in permeability. FcRn-mediated recycling is concentration-dependent and has demonstrated enhanced recycling below 1600 nM in other endothelial cells *in vitro* (Grevys et al. 2018). Accordingly, the permeability of human and mouse IgG was evaluated at concentrations 10-fold lower (66.7 nM) and 5-fold higher (3.33 μM) than that previously tested. No evidence of altered permeability associated with FcRn-dependent shuttling was observed as both IgGs exhibited comparable values at low or high IgG concentrations (Figure 3-3a). We also addressed whether any other IgG-specific mechanisms have the capability to saturate IgG transcytosis. To accomplish this, the permeability of labeled IgGs was measured in the presence of unlabeled human IgG at 1- to 20-fold endogenous serum levels in humans. The presence of any amount of unlabeled human IgG did not significantly alter the permeability of human or mouse IgG (Figure 3-3b), which were again comparable. Based on the lack of concentration-dependent alterations in permeability at nanomolar concentrations or in the presence of unlabeled IgG, IgG transcytosis was not consistent with a saturable phenomenon. Consequently, the internalized amount of fluorescently-labeled IgG was also non-saturable and supports the notion that the endocytosis of IgG occurs via a nonspecific fluid-phase process.

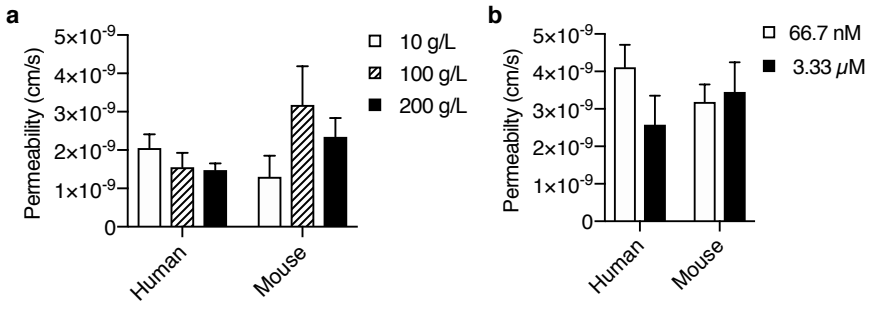

Figure 3-3: IgG transcytosis across iBECs is non-saturable regardless of FcRn engagement. (**a**) The permeability of human and mouse IgG at 667 nM in the presence of 10, 100, or 200 g/L of unlabeled human IgG, or (**b**) at 66.7 nM and 3.33 μM in the absence of unlabeled IgG. Values are the mean of three (a) or four (b) independent differentiations ± SEM, and were compared by two-way ANOVA followed by Sidak's multiple comparison test to determine differences between groups or followed by Tukey's multiple comparison test to determine differences within groups.

3.5.4 Characterization of Saturable RMT of Transferrin

As a comparison to the non-saturable mechanism observed for IgG, we assessed the well-characterized RMT of transferrin observed in vivo, but not currently reported for iBECs (Poduslo, Curran, and Berg 1994; Ribecco-Lutkiewicz et al. 2018). After confirming TfR expression in iBECs (Figure B-2), the permeability of transferrin was evaluated as a function of concentration. Consistent with trends previously observed in literature, the permeability of transferrin decreased with increasing concentration until plateauing at micromolar concentrations (Figure 3-4a). After confirming saturable RMT of transferrin across iBECs, we next investigated whether its intracellular processing was different from that observed for human or mouse IgGs. Additionally, we also addressed whether any differences exist between saturated (667 nM) and non-saturated (66.7 nM) transcytosis regimes for transferrin. Transferrin-containing vesicles exhibited a similar size distribution observed for IgGs, but were significantly more numerous regardless of transferrin concentration (Figure

3-4b,c, and Figure B-4a,b). Similarly, normalized accumulation analyses revealed comparable intracellular accumulation at either transcytosis regime (Figure 3-4d). The accumulation metrics for transferrin were also significantly lower than those observed for mouse IgG (Figure B-4c).

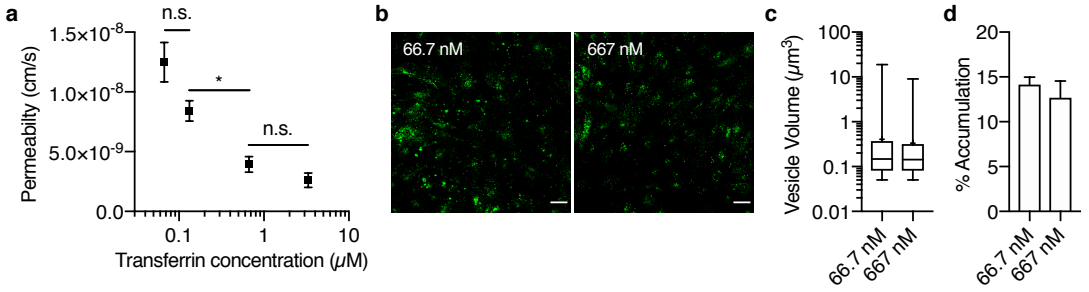

Figure 3-4: RMT of transferrin exhibits saturable kinetics and limited lysosomal shuttling in iBECs. (**a**) The permeability of transferrin at varying concentrations. (**b**) Representative deconvolved Airyscan super-resolution confocal images showing the intracellular vesicular structures containing fluorescently-labeled transferrin at 66.7 or 667 nM (green) in fixed iBECs after a 1-hr pulse. Images are Z-projections based on average intensity, and scale bar represents 20 µm. (**c**) Representative vesicle diameter distribution of transferrin-containing structures. Distributions are from one 192 × 192 μm^2 image for each IgG and shown as boxplots with interquartile ranges and median. The mean is shown as a cross and error bars represent minimum and maximum values. (**d**) Quantification of average vesicle intensity for either concentration of transferrin relative to its inoculum intensity. Values in (a) are the mean from four independent differentiations ± SEM, and were compared using one-way ANOVA followed by Tukey's multiple comparison test (n.s., $P > 0.05$, $*P < 0.05$). Values in (c) and (d) represent means from three independent differentiations ± SEM, where each value is an average from five 192 × 192 μm^2 images, and were compared using two-tailed Student's t-test.

3.5.5 Biophysical Attributes of Macromolecules Influence iBEC Permeability

The plateauing of transferrin permeability indicated that RMT was complemented by a transcytosis mechanism whose rate is concentration-independent, and therefore the amount transported is always proportional to the inoculum

concentration. In agreement with other literature (Watts and Dennis 2013), we hypothesized that this transcytosis mechanism occurred nonspecifically and originated from fluid-phase endocytosis. Such a mechanism would also explain the comparable permeability observed for IgG and its fragments, despite the 32–150 kDa molecular weight (MW) range. However, previous findings have demonstrated the potential for size-dependent differences in BBB permeability *in vivo* (Kutuzov, Flyvbjerg, and Lauritzen 2018; Shi et al. 2014). To investigate whether nonspecific transcytosis of macromolecules across iBECs is size-dependent, we assessed the permeability of 10-kDa dextran because it is above the size limit for paracellular transport at the BBB *in vivo* (Yanagida et al. 2017) and would therefore be transported only by transcytosis. We found that the permeability of 10-kDa dextran was ~2.0×10^{-8} cm/s (Figure 3-5a), nearly an order of magnitude higher than that observed for the 32 kDa Fc. Dextrans could engage specific processes in iBECs similar to that observed for other endothelial cells (Rouleau, Rossi, and Leask 2010), which may have contributed to the increased permeability. Thus, a 155-kDa dextran (which is of comparable size to IgG) was examined. The permeability of the 155-kDa dextran was significantly lower than that of the 10-kDa dextran (Figure 3-5a) and suggested that iBECs dextran-specific interactions did not influence its transcytosis across iBECs. We next investigated whether the small size of 10-kDa dextran contributed to its increased permeability by assessing a comparably sized 14-kDa alpaca-derived single-domain antibody (sdAb), which targets a non-human antigen (green fluorescent protein). Despite only a 4 kDa difference in MW, the permeability of the sdAb was nearly 4-fold lower than that observed for the 10-kDa dextran (Figure 3-5a). This finding suggested that size was likely not an important factor for the rapid transcytosis of 10-kDa dextran.

Interestingly, comparing the permeabilities of the sdAb and larger macromolecules revealed a marginal, but significantly higher, permeability for the sdAb (Table 3-1).

Enhanced permeability of certain sdAbs across the BBB *in vitro* has been reported previously and was attributed to highly positively charged isoelectric points (pI >9) (T. Li et al. 2012), which is hypothesized to foster adsorptive interactions with the negatively charged luminal surface of the BBB to facilitate transcytosis (Goulatis and Shusta 2017). We performed isoelectric focusing (IEF) of the sdAb as well as 10- and 155-kDa dextrans to explore whether there were disparities in charge that might explain their enhanced permeability. Gel-based IEF revealed that both the 10-kDa dextran and sdAb exhibited a pI outside the standard range used (>9.6); whereas, the 155-kDa dextran exhibited a wide distribution that centered predominantly on a pI range of 7.0–9.6 (Figure 3-5b). Accordingly, these observations support the role of charge in the increased transcytosis of both the sdAb and 10-kDa dextran as all the other macromolecules with lower permeability values exhibit a pI near or below the medium pH of 7.4 (Table 3-1).

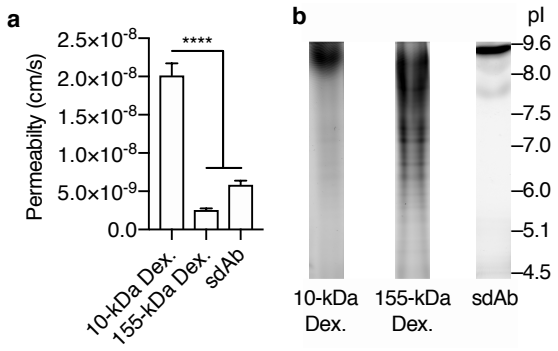

Figure 3-5: IEF reveals charge-dependent increase in iBEC permeability of a dextran and sdAb. (**a**) The permeability of 10-kDa and 155-kDa dextrans and a sdAb. (**b**) IEF images for the three macromolecules. Selected pI values from a concurrently run standard are shown on the right. Values in (a) is the mean from four independent differentiations ± SEM, and were compared using one-way ANOVA followed by Tukey's multiple comparison test (****P < 0.0001). The lanes have been cropped from two images of a gel excited using different excitation and emission settings (Figure B-6).

	Molecular Weight (Approximate)	Isoelectric Point	iBEC Permeability ($\times 10^{-9}$ cm/s)	Abluminal Accumulation (% in 1 hour)	Multiple Comparisons
Human IgG	150 kDa	6.6–9.0	2.24 ± 0.63	0.16	A
Mouse IgG	155 kDa	5.5–8.0	1.30 ± 0.51	0.09	A
Human Fc	32 kDa	4.5–6.5	2.34 ± 0.73	0.17	A
Human Fab	50 kDa	7.5–9.0	2.89 ± 1.48	0.21	A
Human transferrin	80 kDa	5.2	2.62 ± 1.21	0.19	A
10-kDa dextran	10 kDa	>9.6	20.30 ± 2.31	1.48	B
155-kDa dextran	155 kDa	7.0–9.6	2.50 ± 0.30	0.18	A
Alpaca sdAb	14 kDa	>9.6	5.85 ± 1.11	0.43	C

Table 3-1: Summary of iBEC permeability values and select biophysical attributes of various macromolecules. The pI of the dextrans (10 and 155 kDa) and sdAb are derived from Figure 3-5b, and references for select pI values are noted in parentheses. Permeability values are the mean from four unique differentiations, except for the Fab and Fc that were from three, ± SEM. The percentage of macromolecules initially added to the luminal compartment that accumulated in the abluminal compartment (after 1 hour) is provided as "Abluminal Accumulation (% in 1 hour)". All analyte concentrations are 667 nM. The permeability values were compared using one-way

ANOVA followed by Tukey's multiple comparison test. Means within the same group are not significantly different ($P > 0.05$).

3.6 Discussion

Currently, the mechanisms influencing the limited transcytosis of IgG across BECs remain unclear. Prevailing views suggest either a nonspecific or receptor-mediated mechanism, which often implicates FcRn given its ability to shuttle IgG bidirectionally to either cell surface. Our observations are consistent with a transcytosis mechanism that is independent of FcRn-mediated processes and does not exhibit a saturable phenomenon. Accordingly, we propose that IgG transcytosis across BECs occurs by a nonspecific process originating from fluid-phase endocytosis, in agreement with other conclusions including a recent report by our group demonstrating reduced IgG uptake via macropinocytosis inhibition (Mantle and Lee 2019; Yu and Watts 2013). To assess the influence of FcRn-mediated processing, we used a comparative IgG-based approach, similar to a previous *in vivo* report (Yip et al. 2014), which exploits the well-characterized stringency of human FcRn to only bind a unique sequence present on the Fc domain of some IgGs (Ober et al. 2001; Ward et al. 2003). Visualization and quantification of transcytosis within the same timeframe was achieved by using our previously developed *in vitro* BBB model that consists of a monolayer of iBECs on a COL1-based hydrogel (Ruano-Salguero and Lee 2018). We observed that despite significant differences in lysosomal accumulation that was consistent with preferential FcRn-mediated recycling (Ward et al. 2003), all tested IgGs exhibited comparable iBEC permeability. As there was no evidence supporting RMT of IgG by FcRn, we assessed whether FcRn or any other IgG-specific receptor or mechanism could indirectly alter its permeability by performing concentration-dependent and inhibitory studies. The permeability of IgG was concentration-

independent, even at levels near the dissociation constant of human FcRn (Neuber et al. 2014), and was also non-saturable regardless of its ability to engage FcRn. Thus, there was no apparent contribution from FcRn or other potential IgG receptors. Tripartite motif-containing protein 21 (TRIM21) was detected in iBECs (Figure B-2), but it is known to mediate the ubiquitination of IgG-antigen complexes (Rhodes and Isenberg 2017) and no reports suggest it contributes to IgG transcytosis. The expression of TRIM21 remains to be confirmed *in vivo*, but it may be the unidentified IgG-associated protein previously reported in BECs because of its comparable MW (Deane et al. 2005). Fc γ receptor IIb can also mediate the RMT of IgG (Ishikawa et al. 2015), however its expression was not detectable in iBECs (Figure B-2) and remains unknown in BECs. Taken together, these results show that intracellular processes, including lysosomal degradation and FcRn-mediated recycling, do not indirectly influence the iBEC permeability of IgG.

An inherent complication of studies demonstrating saturable, or non-saturable, transcytosis of IgG across the BBB *in vivo* is the common practice of using cerebrospinal fluid (CSF) as a surrogate for the interstitial fluid (ISF) tzhat surrounds brain parenchyma. Although CSF captures the levels of macromolecules in ISF via ISF-to-CSF convective-driven exchange (Hladky and Barrand 2018), it also captures the entry of macromolecules across the less restrictive (relative to the BBB (Pardridge 2016)) endothelium and epithelium that forms the blood-CSF barrier (BCSFB). Thus, it is possible that any saturable transcytosis mechanism for IgG may be attributed to the BCSFB,(Griffin and Giffels 1982), which also expresses FcRn and warrants further examination of its potential role (Pyzik et al. 2019). However, an overlooked observation is that the steady-state CSF-to-serum levels of IgG3 in humans is at the

same proportion as the other three IgG subclasses despite a lack of strong FcRn engagement (Kaschka et al. 1979). Comparable CSF-to-serum levels between the human IgG subclasses support our conclusion that transcytosis across BECs is FcRn-independent, but also indicate that FcRn at the BCSFB may not significantly contribute to any preferential transcytosis at steady-state. Based on experimental limitations, the present study could not directly address the factors that influence brain-to-blood IgG transport across iBECs, which may include FcRn-mediated processes (Cooper et al. 2013; Deane et al. 2005).

Development of new approaches to increase the penetration of IgG or other macromolecules across the BBB can benefit from thorough *in vitro* characterization to appropriately interpret transcytosis phenomena. Our observation of saturable transcytosis of transferrin is consistent with other *in vivo* and *in vitro* reports also examining RMT by the TfR (Alata et al. 2014; Villaseñor et al. 2017) and the increased intracellular accumulation (relative to human IgG) supports the notion that lysosomal accumulation and degradation is a detriment to RMT (Villaseñor et al. 2017). Although TfR saturation in iBECs (~667 nM transferrin) is similar to that observed in mice (~500 nM of an anti-transferrin IgG (Alata et al. 2014)), saturation kinetics can vary from species to species (Yu et al. 2014). Accordingly, evaluation of other RMT receptors should consider appropriate species-relevant models and potential saturation by native ligands at endogenous levels. As demonstrated here using Airyscan technology, the relatively low levels of transferrin and IgG accumulation suggest assessment of other transcytosis kinetics would also benefit from the added improvements in sensitivity and resolution facilitated by super-resolution confocal microscopy (Villaseñor et al. 2017). An important corollary of the

saturation kinetics observed for transferrin is that any enhanced BEC permeability via RMT can eventually saturate and exhibit a nominal transcytosis rate. Because of the comparable permeability of antibodies (150 kDa), 155-kDa dextran, transferrin (80 kDa) at saturation, and Fab (~50 kDa) and Fc (~32 kDa) IgG fragments (Table 3-1), we propose that this nominal transcytosis rate likely originates from nonspecific fluid-phase endocytosis because it is constitutive and concentration-independent. Although other studies using dextrans of varying MW have presented evidence suggesting BBB permeability is size-dependent (Shi et al. 2014; Kutuzov, Flyvbjerg, and Lauritzen 2018), our observations for the sdAb (14 kDa) and 10-kDa dextran suggest charge is a more important determinant of BEC permeability. Dextrans derived from different bacterial sources or with varying chemical modifications may vary in charge and require thorough characterizations before interpreting BEC permeability given the importance of charge on BEC transcytosis (Goulatis and Shusta 2017). Because the highly basic charges of the sdAb and 10-kDa dextran were indistinguishable using IEF, it is possible that their drastic differences in permeability are attributable to potentially small or large differences in pI (Griffin and Giffels 1982). Other biophysical attributes can also alter BBB permeability similar to that reported for cell-penetrating peptides (Stalmans et al. 2015). Interestingly, dextrans with a MW 10 kDa or less can exhibit a random coil conformation (Granath 1958), which suggests that low MW dextrans may also influence BEC permeability via conformation. As charge and conformation-based alterations in the BBB permeability of macromolecules may not necessarily exhibit saturable phenomena (Stalmans et al. 2015), a lack of *a priori* biophysical characterization may lead to misclassifications of transcytosis mechanisms.

In summary, our findings demonstrate that IgG transcytosis across an *in vitro* BBB exhibits a non-saturable and nonspecific mechanism, and supports the use of RMT approaches or modifications of biophysical properties, such as pI, to achieve improved brain uptake of therapeutic IgGs (Goulatis and Shusta 2017). Additionally, this study also supports the use of *in vitro* BBB models, in combination with thorough biophysical characterizations, to provide useful assessment of therapeutic candidates before translation to preclinical models.

Chapter 4

ADSORPTIVE-MEDIATED ENDOCYTOSIS OF SULFO-Cy5-LABELED IgG CAUSES ABERRANT IgG PROCESSING BY BRAIN ENDOTHELIAL-LIKE CELLS

4.1 Preface

This chapter is adapted from: Ruano-Salguero JS and Lee KH. (2020) Adsorptive-mediated endocytosis of Sulfo-Cy5-labeled IgG causes aberrant IgG processing by brain endothelial-like cells, with permission (see Appendix D).

In this chapter, the utility of coupling permeability screening with biophysical characterizations is demonstrated with respect to the impact of fluorescent labeling on IgG transport. Analysis of intracellular accumulation and FcRn-IgG binding kinetics were employed to investigate the modulation in transport rate and processing of fluorescently labeled IgG.

We like to thank Dr. Jefferey L. Caplan and the staff at the Bioimaging Center at the Delaware Biotechnology Institute for technical assistance with confocal and super-resolution microscopy. This work was funded in part by an NSF GRFP fellowship (Award Number 1247394). Microscopy access was supported by grants from the NIH-NIGMS (P20 GM103446), the NSF (IIA-1301765) and the State of Delaware.

4.2 Abstract

Brain endothelial cells (BECs) hinder macromolecules from reaching brain parenchyma, necessitating the evaluation and engineering of therapeutic immunoglobulin γ (IgG) for improved brain delivery. Emerging fluorescent-based approaches to assess IgG brain exposure can expedite and complement current methods, however alterations in IgG pharmacokinetics following fluorophore conjugation, which remain unexplained, indicate that conjugation may confound analysis of native IgG processing. Here, changes in transcytosis and intracellular processing of IgG conjugates (with sulfonated cyanine 5) were examined using human induced pluripotent stem cell-derived BECs (iBECs). Above a critical degree of labeling, transcytosis rates increased significantly but could be attenuated by nonspecific protein competition. Concurrent increases in intracellular accumulation, which was not attributable to disrupted binding by the neonatal Fc receptor (FcRn), are indicative of indirect reduction of FcRn-mediated recycling that agree with reported aberrations in the pharmacokinetics of certain unconjugated IgGs. Overall these findings support the notion that certain fluorophore-IgG conjugates can engage adsorptive-interactions with cell surface moieties, reminiscent of phenomena exhibited by cationized IgG, and provide *in vitro* criteria to identify changes in IgG processing following fluorophore conjugation.

4.3 Introduction

Inefficient brain delivery of immunoglobulin γ (IgG)-based therapeutics represents an additional challenge to the development of first-in-class immunotherapies for brain diseases (Watts and Dennis 2013). The cerebral endothelium that forms the main structural component of the blood-brain barrier

(BBB) limits most proteins, including endogenous IgGs, from entering brain parenchyma to an appreciable extent (Zhao et al. 2015). At the cellular-level, the reduced vascular permeability that differentiates cerebral from peripheral endothelium is attributed to the limited vesicular trafficking of brain endothelial cells (BECs) (Ayloo and Gu 2019). Accordingly, recent investigations into the trafficking of therapeutic and endogenous IgGs have begun to provide an improved understanding of the processes that influence their endosomal fate and transcytosis across BECs (Haqqani et al. 2018; Villaseñor et al. 2017). Likewise, complementary studies of BEC permeability help to correlate the relationship between endocytic pathways and transcytosis rates (Haqqani et al. 2018). With increased recognition on the importance of analyzing IgG processing by BECs, future assessments of therapeutic IgGs for improved brain penetration can benefit from continued advancements in methodologies to rapidly and accurately characterize their interactions with BECs.

Pioneering applications of fluorescence microscopy and tomography to assess BEC permeability and brain accumulation/clearance of fluorescently-labeled therapeutics represent emerging and beneficial approaches to investigate brain delivery *in vivo* (Shi, Zeng, and Fu 2014; Kutuzov, Flyvbjerg, and Lauritzen 2018; S. Li et al. 2017). However, increased adoption of these high-throughput and minimally-invasive technologies to study tissue distribution and target engagement of therapeutic IgGs in related fields have also highlighted the potential for changes in IgG processing (Debie and Hernot 2019). Although not well understood, the conjugation of fluorophores to IgG can increase nonspecific tissue deposition that results in premature catabolism, leading to reduced serum half-life (Sato et al. 2015). Pre-screening of fluorophore-IgG conjugates for irregular pharmacokinetics is therefore

recommended, however subtle cellular-level changes may remain undetected. Moreover, similar phenomena reported for radio-labeled IgGs suggest changes in BEC processing of IgG are likely amplified because of their limited vesicular trafficking (Bickel 1995). With continued advancements in fluorescence-based technologies spurring new applications in brain delivery studies, an improved understanding of fluorophore-specific changes in IgG-BEC interactions is needed.

Investigations into the aberrant pharmacokinetics of other IgG conjugates suggest fluorescent labeling can occasionally mediate increases in nonspecific cellular uptake. Increased endocytosis of certain conjugated (e.g. polyamines) and unconjugated IgGs are often attributed to the introduction of highly positive-charged patches on IgG that mediate adsorptive interactions with negatively charged cell surface moieties via adsorptive-mediated endocytosis (AME) (Datta-Mannan, Thangaraju, et al. 2015; Triguero, Buciak, and Pardridge 1991). Accordingly, induction of similar phenomena following the conjugation of negatively charged hydrophobic fluorophores has not been investigated. However, recent reports have demonstrated that macromolecules conjugated with negatively charged hydrophobic molecules can elicit increased cellular uptake via an AME pathway distinctive from that of highly cationic macromolecules (Voigt, Christensen, and Shastri 2014). Consistent with charge-dependent phenomena, fluorophores with higher electronegativity reduce the degree of labeling (DOL) required to cause detrimental IgG pharmacokinetics (Sato et al. 2015; Triguero, Buciak, and Pardridge 1991). These recent findings suggest fluorescently-labeled IgG induces anionic-enhanced AME, which may lead to similar alterations in transcytosis across BECs for cationized IgG (Triguero, Buciak, and Pardridge 1991). Additionally, it remains unclear whether

fluorophore conjugation also disrupts the neonatal Fc receptor (FcRn)-mediated recycling of IgG, a ubiquitous function of all endothelial and epithelial cells (Ward and Ober 2018), that contributes to its favorable pharmacokinetics (i.e. long serum half-life). Direct or allosteric disruption of FcRn binding to fluorescently-labeled IgG may therefore represent a parallel alteration in IgG processing that contributes to the irregular pharmacokinetics often observed.

Here, we examined the influence of fluorophore conjugation, particularly the DOL, on IgG processing and transcytosis by using induced pluripotent stem cell-derived BECs (iBECs) and a quantitative BBB model that couples permeability measurements with intracellular analysis (Ward and Ober 2018; Ruano-Salguero and Lee 2018, 2020). Sulfonated cyanine 5 (Sulfo-Cy5) was used as a representative fluorophore for its common traits (e.g. sulfonated, cyanine derivative) and previous evaluation *in vivo* (Schneider et al. 2017). Our findings reveal that fluorescently-labeled IgG, above a critical DOL, exhibits increased iBEC permeability and intracellular accumulation. These findings highlight the importance of characterizing fluorophore-IgG conjugates for aberrant cellular processing, especially with respect to BECs.

4.4 Methods

4.4.1 Fluorophore Conjugation to IgG

Pooled human IgG (Gammagard Liquid Immune Globulin Intravenous, Baxter) was dialyzed in phosphate buffered saline (PBS) to remove glycine in the storage formulation. A 0.1 M sodium bicarbonate solution was added to 2 g/L of IgG at 1/10th the reaction volume. A N-hydroxysuccinimide ester-activated Sulfo-Cy5

(Lumiprobe) was dissolved in dimethyl sulfate (MilliporeSigma) to a concentration of 10 g/L, and was added to the IgG at varying IgG:fluorophore molar ratios (from 1:5 to 1:40). The resultant solution was gently mixed for one hour using a vertical tube rotator. Meanwhile, a PD Miditrap G-25 (GE Healthcare) desalting column was equilibrated in PBS with 2 mM sodium azide according to the manufacturer (centrifugation protocol). Afterwards, the fluorescent solution was added to the spin column, centrifuged, and the resultant eluate was collected. For the 1:20 and 1:40 molar ratio solutions, a serial purification using three desalting columns were used to remove excess fluorophore. Each fluorophore-IgG conjugate solution was then concentrated using a 2.5 kDa MW cutoff spin column to a final concentration above 5 g/L. To assess the DOL, the IgG conjugates were analyzed via standard spectroscopic methods (DS-11+ Spectrophotometer, DeNovix). An excitation wavelength of 642 nm was used to measure the absorbance values at 280 and 662 nm. The DOL was calculated according to the manufacturer with a molar extinction coefficient of 271000 $L \cdot mol^{-1} \cdot cm^{-1}$ and a 280 nm correction factor of 0.04. Qualitative assessment to verify increasing DOL and consequential decreasing isoelectric point (pI) was performed via isoelectric focusing (Figure C-1) as previously described (Ruano-Salguero and Lee 2020). Briefly, a pH 3–10 Criterion IEF Precast Gel (Bio-Rad) was loaded with approximately 2 µg of DOL3/6 and 10 µg of DOL14 conjugate per lane and a 4.45–9.6 pI standard (Bio-RaD). The gel was run in a Criterion cell (Bio-Rad) according to the manufacturer's protocol and imaged using a Typhoon FLA-7000 scanner (GE Healthcare Life Sciences). Afterwards, the pI standard was visualized with SYPRO Ruby (Invitrogen) using the 'Rapid' protocol provided by the manufacturer.

4.4.2 Hydrogel-based iBEC Experimental System

Collagen type I from rat tendon (Corning) was prepared as a hydrogel and conjugated on 8-chambered glass coverslips based on methods extensively described (Ruano-Salguero and Lee 2018, 2020). IMR90-4 iPSCs (WiCell) were cultured and differentiated to BEC-like cells as previously described (Ruano-Salguero and Lee 2018, 2020). All experiments were performed on the second day of subculture. The culture medium was replaced on both days post-subculture.

4.4.3 Live-cell Permeability Measurements

IgG conjugates were diluted to 0.1 g/L in Phenol-free Ham's F-12 (Caisson). Sodium fluorescein (NaFL) (2 μM) was used as an internal control to assess barrier integrity. For the competitive assays, serum or unlabeled IgG were added to the IgG conjugates before dilution. Following media replacement on the second day of subculture, the culture medium was aspirated and replaced with a fluorogenic solution. The samples were then immediately mounted in a preheated and humidified enclosure connected to a Zeiss 710 confocal microscope (Zeiss). Images were acquired using a C-Apochromat 40× (NA 1.2) water immersion objective (Zeiss) and acquisition parameters were similar to those previously described (Ruano-Salguero and Lee 2018, 2020). Permeability values were calculated as previously described (Ruano-Salguero and Lee 2018, 2020).

4.4.4 Pulse Assay and Airyscan Imagining/Analysis

Similar to the permeability experiments, the pulse assay involved exposing the iBECs to DOL3 or DOL14 IgG conjugates (0.1 g/L) for one hour. Afterwards, the samples were fixed by adding 16% (v/v) paraformaldehyde (Electron Microscopy Sciences) to a final concentration of 4% (v/v). After 30 minutes the samples were

extensively rinsed with PBS (2 mM sodium azide). Images were acquired using a Zeiss 880 confocal microscope with an Airyscan detector (Zeiss) and a C-Apochromat 40× (NA 1.2) water immersion objective. Within the Zen Black software (Zeiss), Airyscan FAST mode was used at super-resolution (voxel size of 0.0497 × 0.0497 × 0.083 μm^3; 3876 × 3876 × 1 pixel), and acquisition parameters (laser and gain) for DOL3 and DOL14 samples were not changed between replicates. Additionally, the same parameters were used to generate standard curves for each IgG conjugate to normalize RFU values. All related images for each IgG conjugate were batch processed in Zen Black using the same deconvolution parameters. Volocity (Perkin Elmer) was used to quantify 3D object-based statistics (mean object intensity and total count) using a standardized threshold of 2-3 standard deviations of the mean signal.

4.4.5 Quantifying FcRn-IgG Binding

Biotinylated human FcRn (Acro Biosystems) was immobilized on streptavidin biosensors (FortéBio) on an Octet RED96e (FortéBio) according to the manufacturer's protocol. Briefly, the FcRn was resuspended in deionized water to 5 mg/L and the IgG samples were buffer exchanged in pH 6.0 PBS with 0.05% (v/v) Tween-20 (MilliporeSigma) (Sample Buffer). The mouse IgG sample (MilliporeSigma) was directly suspended in the Sample Buffer. The streptavidin biosensors were rehydrated in pH 7.4 PBS for 10 minutes, and were subsequently loaded with FcRn for 60 seconds, at which the baseline-corrected reading was approximately 2.1 nm. The IgG samples (diluted from 2 g/L to 0.3125 g/L) were associated for 300 seconds, and subsequently dissociated in Sample Buffer for 60 seconds. A Sample Buffer only analyte was also used, and the experiment was repeated with new biosensors but no FcRn loading to double reference the data. The temperature was set at 30 ºC and the

data collection rate was 10 Hz. Using the Octet System Data Analysis software (FortéBio), the steady-state responses were calculated to determine the dissociation constant and associated error.

4.4.6 Statistics

Prism 7 (GraphPad) was used for statistical analysis. Comparison of data was performed using Student's t-test, and one/two-way ANOVA with $\alpha = 0.05$. The sample size (minimum of 3 biological replicates, each originating from a unique differentiation) and statistical test is indicated in each figure legend.

4.5 Results

4.5.1 iBEC Permeability of Fluorophore-IgG Conjugates Increases with DOL

To assess the influence of fluorescent labeling on IgG transcytosis across BECs, we measured the permeability of human IgG conjugates with an average DOL of 1 to 14. For low DOL conjugates DOL1 and DOL3, iBEC permeability was not significantly different (Figure 4-1A) and was comparable to values reported for unlabeled human IgG (Ruano-Salguero and Lee 2018). However, iBEC permeability of IgG increased significantly for conjugates with a DOL of 6 and above (DOL6 and DOL14) (Figure 4-1A), which did not lead to elevated paracellular permeability of NaFL (Figure C-2A). Given the significant increase in permeability, we also evaluated the rate of IgG transcytosis for linearity to verify the calculation of permeability and assess any time-dependent phenomena. After normalization to initial luminal relative fluorescent units (RFU) for appropriate comparison, each conjugate exhibited a linear transcytosis profile during the one-hour permeability assay (Figure 4-1B).

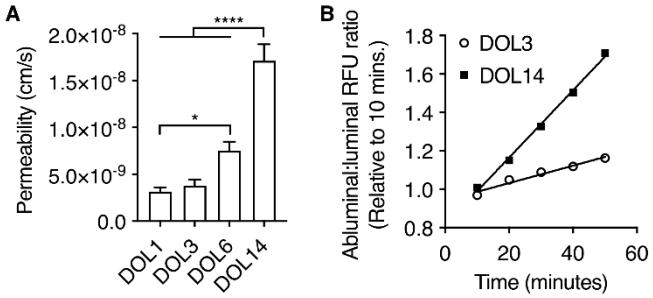

Figure 4-1: DOL-dependent increase in iBEC permeability of fluorophore-IgG conjugates. (A) Permeability of IgG at varying DOL with Sulfo-Cy5. Values represent the mean ± SEM, with N=4. Means were compared using one-way ANOVA followed by Tukey's multiple comparison test (*$p < .05$, ****$p < 0.0001$). (B) Representative abluminal accumulation profile for DOL3/14 IgG conjugates. Values represent abluminal-to-luminal RFUs normalized to the initial reading at 10 minutes.

4.5.2 IgG Transcytosis Mediated by Fluorophore Conjugation is Attenuated by Nonspecific Competition

We examined whether competition with serum proteins would attenuate the nonspecific adsorption phenomena in a manner similar to cationic-enhanced AME (Triguero, Buciak, and Pardridge 1991), based on the hypothesis that the increased transcytosis rate of fluorophore-IgG conjugates is attributable to anionic-enhanced AME. While the DOL3 conjugate did not exhibit significant changes in permeability regardless of serum concentration, the permeability of the DOL14 conjugate was significantly reduced in the presence of 30% serum relative to 5% serum (Figure 4-2A). Attenuation of AME of IgG by serum has also been speculated to involve serum-specific factors with low molecular weights (Triguero, Buciak, and Pardridge 1991); therefore, unlabeled human IgG was used as a high molecular weight alternative as we have previously demonstrated no changes in the permeability of IgG conjugates in the presence of unlabeled IgG at 10-200 g/L (Ruano-Salguero and Lee 2020). Consistent with the attenuation observed for serum, a similar reduction in the

permeability of the DOL14 conjugate was observed with increasing levels of unlabeled human IgG (Figure 4-2B). Neither serum nor unlabeled IgG demonstrated an influence on the paracellular permeability of NaFL (Figure C-2B and Figure C-2C).

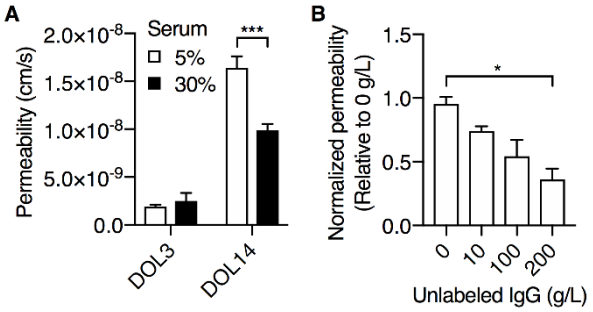

Figure 4-2: Nonspecific protein competition attenuates permeability of high DOL IgG conjugate. (A) Permeability of DOL3/14 IgG conjugates with serum, or (B) the DOL14 IgG conjugate with unlabeled IgG. Values represent the mean ± SEM, with N=4 (A) or N=3 (B). Means were compared using two-way ANOVA followed by Sidak's multiple comparison test (***$p < 0.001$) (A), and one-way ANOVA followed by Dunnett's multiple comparison with 0 g/L as the control.

4.5.3 High DOL Increases Intracellular IgG Accumulation

Based on the large disparity between the iBEC permeability of DOL3 and DOL14 IgG conjugates, we next evaluated if significant changes in intracellular processing also occurred. After one hour of continuous exposure, Airyscan super-resolution microscopy revealed comparable uptake and compartmentalization of both the DOL3 and DOL14 conjugates (Figure 4-3A). However, quantitative analysis that normalizes the intracellular concentrations relative to those during exposure demonstrated that the DOL14 conjugates exhibited approximately 6-fold higher accumulation relative to the DOL3 conjugates (Figure 4-3B).

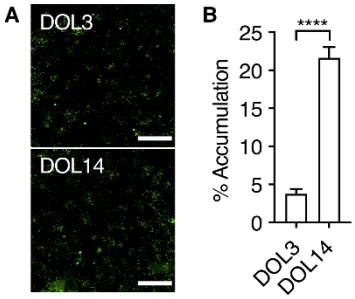

Figure 4-3: High DOL IgG conjugate exhibits increased intracellular accumulation and activity. (A) Representative deconvolved Airyscan super-resolution confocal images (Z-projection average) showing intracellular vesicular structures containing DOL3/14 IgG conjugates (green). Scale bar is 50 µm. (B) Abluminal RFUs normalized to luminal RFUs after exposure to DOL3/DOL14 IgG conjugates for one hour. Values represent the mean ± SEM, with N=4. Each value is an average from five 192 × 192 μm^2 images. Means were compared using paired, two-tailed Student's t-test (****$p < 0.0001$).

4.5.4 FcRn Binding to IgG Conjugates is Unaltered at Low or High DOL

Increases in IgG accumulation within endothelial cells often signifies disruptions in FcRn-mediated recycling of IgG, which suggests fluorophore conjugation at a high DOL either directly or indirectly alters FcRn processing. To evaluate whether the FcRn binding motif on IgG was directly disrupted by the presence of fluorophores, FcRn binding between the low and high DOL conjugates was determined. Additionally, unlabeled human and mouse IgG was used as positive and negative controls, respectively (Ober et al. 2001). Relative to unlabeled human IgG, there was no significant change in the FcRn dissociation constant for either conjugate (Figure 4-4).

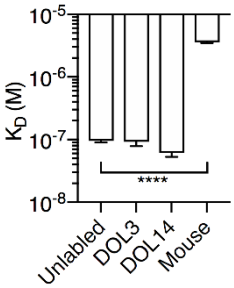

Figure 4-4: Fluorophore conjugation does not alter IgG engagement by FcRn. The calculated dissociation constant (K_D) for unlabeled human (Unlabeled) or mouse IgG (Mouse), and DOL3/14 IgG conjugates. Values represent the mean ± SEM derived the fit using the Octet System Data Analysis software. Means were compared using one-way ANOVA followed by Dunnett's multiple comparison with unlabeled human IgG as the control case (****$p < 0.0001$).

4.6 Discussion

Indirect evidence from several reports suggest the increased tissue deposition and rapid serum clearance observed for certain fluorophore-IgG conjugates is attributable to increased nonspecific cellular uptake via AME. Related changes in intracellular IgG processing remain unknown but may impact transcytosis and FcRn-mediated recycling. Our results show that fluorophore conjugation can result in a simultaneous increase in transcytosis and intracellular accumulation of IgG by iBECs. Consistent with various studies examining the influence of fluorescent labeling of IgG pharmacokinetics, the extent of changes in IgG processing was related to the DOL. Conventional nonspecific conjugation of fluorophores (e.g. amine- or thiol-mediated) produce a heterogeneous population of IgGs with varying DOL (Cilliers et al. 2017), which implicates two convoluted processes for the observed DOL-dependent alterations. Increasing the DOL increases the proportion of conjugates above the critical value at which AME processes can occur, but conjugates with a DOL greater than the critical value may also exhibit an increased propensity to induce anionic-enhanced AME via additive effects, similar to that observed for cationic-enhanced

AME (Hervé, Ghinea, and Scherrmann 2008). Regardless of the exact processes contributing to the observations, varying the DOL revealed a critical range that segmented iBEC permeability values of fluorescently labeled IgG that were comparable or significantly different from that previously reported by our group for unlabeled IgG (Mantle, Min, and Lee 2016). Because each fluorophore may vary in its propensity to induce changes in cellular processing (critical DOL <1 have been reported) (Cilliers et al. 2017), determining the critical DOL for each unique fluorophore-IgG conjugate is paramount to interpreting their cellular processing and pharmacokinetics. High throughput cellular-based screening methods, such as those recently developed (Grevys et al. 2018), may complement *in vivo* methods used to assess the critical DOL of IgG conjugates, and is supported by the comparable critical DOL for Sulfo-Cy5 observed in this study (DOL <4–6) and that reported *in vivo* (DOL <4) (Schneider et al. 2017). Additionally, the nonspecific attenuation of the high DOL conjugate in the presence of other proteins suggests *in vitro* screening of fluorophore conjugates in serum-free conditions may be more sensitive to disruptions in IgG processing relative to current *in vivo* methods. Similar to the hypothesized attenuation of cationic-enhanced AME,[23] the attenuation observed in this study is likely attributable to nonspecific shielding of adsorptive interactions.

Quantitative analysis of intracellular accumulation for low and high DOL IgG conjugates demonstrate that anionic-enhanced AME also alters native IgG processing. Increases in the normalized vesicular concentrations for the DOL14 conjugate, relative to the DOL3 conjugate, is associated with increased lysosomal accumulation based on our previous characterizations (Ruano-Salguero and Lee 2020) and is in agreement with the reduced half-life observed *in vivo* for certain fluorophore-IgGs (Sato et al.

2015). Transport of conjugate fragments from lysosomes did not appear to contribute to the measured permeability because the abluminal accumulation profile was linear and lacked any lag indication of accumulation, fragmentation, and subsequent transport. Increased accumulation of IgG often implicates disrupted FcRn-mediated recycling caused by a lack of FcRn binding (Ward et al. 2003). However, direct binding of immobilized FcRn to IgG was not significantly impacted by the presence of fluorophores. Instead, FcRn binding may be indirectly impeded by competition with adsorptive interactions for fluorophore-IgG engagement. Indirect hindrance of FcRn-mediated recycling has been reported for unconjugated IgGs with charge abnormalities (i.e. cationic patches) (Kelly et al. 2016), and engineered modifications to IgG that improve FcRn affinity partially restored IgG recycling and pharmacokinetics (Datta-Mannan, Lu, et al. 2015). Nevertheless, irrespective of whether there is altered recycling, the concurrent increase in accumulation and transcytosis are not mutually dependent. For example, we recently demonstrated that mouse IgG exhibits high levels of accumulation relative to human IgG, but there is no associated increase in transcytosis because they are both endocytosed via pinocytosis (Ruano-Salguero and Lee 2020). Accordingly, the increased transcytosis for the high DOL IgG conjugate likely relates to increases in the cell surface concentration via adsorptive interactions, similar to that hypothesized for cationized IgG via cationic-enhanced AME (Ober et al. 2001).

4.7 Conclusions

Fluorescent labeling of IgG offers benefits to the characterization of brain delivery in a manner that is high-throughput and minimally invasive relative to traditional methods. However, the conjugation of fluorophores has the unpredictable

tendency to alter IgG pharmacokinetics, which is indicative of alterations in intracellular processing. In this study, a DOL-dependent increase in the transcytosis of fluorescently labeled IgG across iBECs exemplify the necessity in determining the critical DOL that begins to alter native IgG processing before IgG conjugates are used *in vivo*. Correlations with respect to DOL are not recommended, and physicochemical properties (i.e. electronegativity) may not necessarily represent generalizable descriptors of a fluorophores tendency to alter IgG pharmacokinetics. Finally, the concurrent alterations in IgG recycling is supported by the detrimental pharmacokinetics often observed for fluorophore-IgG conjugates, and indicates that implementation of anionic-enhanced AME, or other forms of AME, for improved brain uptake have to consider reduced IgG half-life as well as nonspecific tissue delivery.

Chapter 5

CONCLUSIONS AND FUTURE WORK

5.1 Summary of Conclusions

Although the antagonization of pathogenic amyloid fibrils with IgG may represent the first disease-modifying therapy for dementia, the high IgG concentrations required to achieve sufficient target engagement within the brain raise concern for treatment cost and accessibility. Efforts to reduce dose concentrations have investigated the mechanisms that impede IgG transport across the BECs that form the BBB. Conflicting findings from animal studies, often pertaining to the role of the FcRn IgG receptor, illustrate the challenges of probing IgG-BEC interactions *in vivo* and have therefore necessitated *in vitro* approaches. While the identification of cultured BECs with IgG transport rates comparable to *in vivo* measurements (i.e. iBECs) has enabled preliminary studies of processes governing the transport of IgG by BECs, conventional experimental systems (i.e. cell culture inserts) and the lack of methods to quantify transport and intracellular processing of IgG at nanomolar concentrations hinder further characterizations, particularly relating to FcRn. In this thesis, a hydrogel-based *in vitro* BBB model and corresponding live-cell and super resolution fluorescence microscopy-based assays were developed to characterize the relationship between processing and transport for IgG as well as other small and large molecules. The methodologies and findings generated here can aid the assessment and development of modified IgGs for improved penetrance across BECs, which may improve the economic feasibility and democratization of IgG therapies for dementia.

In Chapter 2, a COL1 hydrogel-based *in vitro* BBB model was developed to enable the visualization and quantification of cellular permeability at nanomolar concentrations. To realize a COL1 hydrogel that enables the formation of a confluent iBEC monolayer and is compatible with live-cell fluorescence microscopy, various hydrogel formation protocols and COL1-to-glass conjugations were assessed. Initial immunocytochemical characterizations of iBECs on the resultant COL1 hydrogel demonstrated typical BBB marker localization and undisrupted tight junction formation, which indicated proper cell-cell association and monolayer formation. Complementary functional assessment of iBECs on the COL1 hydrogel was achieved by measuring the permeability of benchmark small and large molecules and comparing the values with those reported for iBECs on cell culture inserts. Here, the cellular permeability quantification was achieved with live-cell fluorescence microscopy, which required optimization. Based on the comparable permeability of small and large molecules, including IgG, between iBECs on COL1 and inserts, the COL1-based BBB model was applied to examine IgG transport in the subsequent work presented in this thesis.

In Chapter 3, the uncertain influence of FcRn-IgG interactions on the transcytosis of IgG across BECs was examined. Comparative studies using IgGs that were either recognized or unrecognized by FcRn – based on differing FcRn-binding consensus sequences on the Fc region – was used to assess the consequences of FcRn-IgG interactions. Initially, differential IgG processing between the two IgGs was evaluated by quantifying any differences in lysosomal shuttling and accumulation attributable to FcRn-mediated recycling. Despite no apparent differences in lysosomal shuttling, as evidence by comparable lysosome-IgG colocalization, significant

deviations in average vesicle concentrations between the recognized and unrecognized IgG confirmed that FcRn was only recycling the recognized IgG. However, no differences in permeability between the two IgGs indicated that neither recycling nor lysosomal accumulation influences IgG transcytosis across iBECs. Complementary permeability measurements of both IgGs at nanomolar and micromolar concentrations indicated that IgG transcytosis rates were independent of concentration. Inhibitory experiments with excess IgG (i.e. 100 g/L) corroborated that IgG transport was independent of concentration. Comparative studies with other macromolecules, which varied in molecular weight and active/passive transport pathways, indicated that the transport rate across iBECs for IgG and most other macromolecules is dictated by the rate of nonspecific macropinocytosis, as this endocytosis pathway is both size and concentration-independent. Yet, certain macromolecules exhibited faster transport rates than most of the examined macromolecules, which was attributed to the induction of adsorptive endocytosis based on elevated isoelectric points.

In Chapter 4, the potential of fluorescent labeling to alter the native processing of IgG across BECs was evaluated. Permeability measurements of fluorescently-labeled IgGs with varying DOL demonstrated an increasing rate of transport for IgGs above a critical DOL. Intracellular accumulation analysis revealed significant differences between IgGs with low or high DOL, which indicated that FcRn-mediated recycling of IgG was disrupted when transport rates increased. The disruption in recycling was assessed with FcRn-IgG binding measurements and demonstrated that fluorescent labeling did not directly impede FcRn binding, indicating that strong adsorptive interactions between labeled IgG and the endosomal membrane indirectly hinders FcRn engagement. Suspecting adsorptive phenomena as the basis for the

increased permeability of IgG with a high DOL, the charged moieties on the luminal surface of iBECs were competitively occupied with serum proteins. Only the iBEC permeability of IgGs with a high DOL, not a low DOL, was attenuated with increasing serum concentrations and supported the hypothesis that fluorescent labeling can induce adsorptive endocytosis similar to other small-molecule modifications (e.g. cationization).

5.2 Recommendations for Future Work

5.2.1 Alterations of BBB Permeability with Age

BBB breakdown is emerging as a presumptive triggering event for many neurological disorders, including dementia. The identification of the processes that initiate BBB breakdown remains elusive because any pathogenic changes to one component of the neurovascular unit (NVU) – BBB, astrocytes, pericytes, neurons, basement membrane, brain parenchyma, etc. – can stimulate damage to other components (Sweeney et al. 2018). For example, the symbiotic relationship between pericytes and the BBB can result in self-sustaining and mutual pathological insults if either begins to erode first (e.g. pericyte reductions caused by neuroinflammation can initiate BBB deregulation) (Montagne et al. 2020). However, recent studies suggest alterations in BBB permeability, via reductions in paracellular and transcellular integrity, occurs through yet to be understood age-specific processes independent of pathological insults (A. C. Yang et al. 2020). Because of the interconnected relationships between members of the NVU, the elucidation of age-specific changes relating solely to the BBB remain difficult to examine *in vivo*.

An extension of the *in vitro* work described in this thesis can enable a sensitive and quantitative analysis of paracellular and transcellular transport alterations that are attributed solely to BBB- and age-specific processes. An initial challenge in assaying age-specific changes is obtaining iPSCs generated from young and healthy donors. The accessibility of iPSCs from academic, government, or private repositories can enable the sourcing of iPSCs with patient information (e.g. age, sex, and known diseases) and validation of pluripotentcy via karyotype and multi-germ layer differentiation documentation. An assessment of iBECs generated from young and old iPSCs would be initiated with immunocytochemical analysis for key BBB markers as described in Chapter 2. To track potential permeability alterations originating from either a paracellular or transcellular route, a multiplexed assay with fluorescent probes of varying size and transport pathway (e.g. NaFL, transferrin, and IgG) can be developed based on the permeability assay for macromolecules that incorporates a paracellular integrity control described in Chapter 3. Proteomic assessment of iBECs derived from young, middle-aged, and old donors – via western analysis or two-dimensional gel electrophoresis – can help identify the pathways involved with age-associated changes in BBB permeability. Finally, additional work to corroborate potential BBB-disrupting pathways can assess the consequences of pathway modulation (e.g. knockdown or knockout of associated proteins) on iBEC permeability.

5.2.2 Vascularized BBB Model

Although static *in vitro* BBB models, such as that described in this thesis, facilitate the elucidation of fundamental intracellular processes influencing paracellular and transcellular transport across the BBB, contributions of fluid flow on

the observed phenomena remain unknown and could result in an incomplete description of transport at the BBB. Because altered or disrupted cerebral blood flow is deleterious to the BBB and other components of the NVU *in vivo (*e.g. stroke, hypertension, or brain tumors) (Kisler et al. 2017), next-generation BBB models that recapitulate the vascularized nature of the native BBB can enable investigations on the relationship between fluid flow and BBB functionality. For example, vascularized BBB models have demonstrated the ability of fluid flow to reduce the permeability of both small and large molecule tracers (Grifno et al. 2019). Current hypotheses suggest that these improvements in barrier integrity are predominately attributable to reductions in paracellular leakage, as evidenced by potential tight junction remodeling observed when the cellular monolayer is orientating to the direction of shear (DeStefano et al. 2017). However, based on comparable studies performed on various endothelial cells of the periphery, BECs under fluid flow may also exhibit alterations in transcellular transport that are concomitant with paracellular barrier improvement.

Assessing potential alterations to the active or passive endocytosis pathways that underpin transcellular transport across BECs requires the integration of a vascularized BBB model with cellular-level assays that deconvolute the contributions of paracellular and transcellular transport. Strategies to investigate modulations in endocytosis, such as those that rely on detecting and comparing internalization rates, are available (He et al. 2018), but a simultaneous assessment of permeability is required to decouple concomitant modulations in paracellular leakage. One potential approach would compare the permeability and average vesicular concentrations of molecules transported via an endocytic route to gauge changes in paracellular/transcellular transport rates and alterations in endocytosis rates,

respectively. In particular, investigations using macromolecules that vary in size (12-155 kDa, described in Chapter 3) would enable the detection of size-dependent reductions in permeability indicative of paracellular alterations. Alterations in transcellular transport could be detected via proportionate/disproportionate alterations in the average vesicle concentration between these molecules and the small molecule SR101 (606 Da, described in Chapter 2) that exhibits vesicular compartmentalization. Because receptor- or adsorptive-mediated transcellular transport necessitates interactions between the engaging ligand and corresponding cell surface moieties, fluid flow along the cell surface may be particularly impactful. The challenge in performing the aforementioned studies is the selection of a vascularized BBB model amendable with the live-cell microscopy-based transport and trafficking assay described in Chapter 2 and Chapter 3. Preliminary work using with the Slater group demonstrated the utility of photoablation-based patterning to generate microchannels within PEG diacrylate (PEGDA)-based hydrogels. To enable cellular adherence, the RGDS peptide was incorporated, and enabled the vascularization of the microchannel with immortalized murine BECs (Figure 5-1). Although the system is amendable with microscopy, a substantial reduction in hydrogel volume is needed to enable the quantification of macromolecular transport across iBECs, which remains a challenge for comparable platforms (Grifno et al. 2019).

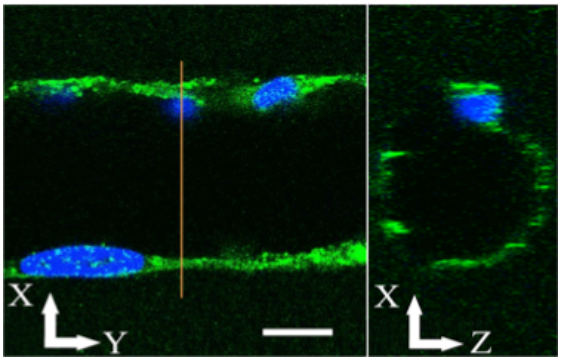

Figure 5-1: Immunocytochemistry of murine BECs (bEnd.3) grown in photoablated-microchannels generated within a PEGDA-RGDS hydrogel. Cells were stained for the tight junction protein zonula occludens-1 (green) and nuclei were stained with DAPI (blue). The right panel is the corresponding x-z cross-section along the orange line shown in the left panel. Scale bar represents 20 µm.

5.2.3 Contributions of the Glycocalyx on Transcytosis at the BBB

Although mutli-omic approaches have identified key processes that establish the restrictive BBB phenotype of BECs, e.g. the Mfsd2a-mediated modulation in lipid bilayer composition that suppresses macropinocytosis (Ayloo and Gu 2019), nonconventional components of the BBB not assessed by traditional multi-omics methods remain understudied, such as the glycocalyx. The BBB and other peripheral endothelium contain a glycocalyx, which is the brush-like lining on the luminal cell surface derived from transmembrane proteoglycans. However, the glycocalyx coverage at the BBB is nearly 8-fold higher than in other endothelium (Ando et al. 2018). The polysaccharide-rich composition of the glycocalyx has directly been implicated in the adsorptive endocytosis at the BBB (Hervé, Ghinea, and Scherrmann 2008), but its potential influence on other transcellular transport processes has only recently been appreciated (Kutuzov, Flyvbjerg, and Lauritzen 2018). In this regard, the ability of the glycocalyx to modulate nonspecific macropinocytosis or receptor-mediated endocytosis (e.g. by the transferrin receptor) remains unexamined.

The visual and sensitive methods to assess transport across BECs developed in this thesis can be leveraged to identify the direct influence of the glycocalyx on passive and active transport. Initially, an assessment of the glycocalyx thickness and composition in iBECs can be performed to establish a baseline comparison with metrics reported with the BBB *in vivo* (Fan et al. 2019). To assess the influence of the glycocalyx on transport, the major constituents of the glycocalyx (i.e. heparan sulfate, chondroitin sulfate, and hyaluronic acid) can be removed with enzymatic treatment (Zeng et al. 2012) and the permeability of untreated and treated iBECs can be systematically compared. Accordingly, the assessment of non-specific and receptor-mediated endocytosis can be obtained by measuring and comparing the permeability of the macromolecules described in Chapter 2.

REFERENCES

Abuqayyas, Lubna, and Joseph P. Balthasar. 2013. "Investigation of the Role of FcγR and FcRn in MAb Distribution to the Brain." *Molecular Pharmaceutics* 10 (5): 1505–13. https://doi.org/10.1021/mp300214k.

Aday, S., R. Cecchelli, D. Hallier-Vanuxeem, M. P. Dehouck, and L. Ferreira. 2016. "Stem Cell-Based Human Blood-Brain Barrier Models for Drug Discovery and Delivery." *Trends in Biotechnology* 34 (5): 382–93. https://doi.org/10.1016/j.tibtech.2016.01.001.

Alata, Wael, Sarah Paris-Robidas, Vincent Emond, Fanchon Bourasset, and Frédéric Calon. 2014. "Brain Uptake of a Fluorescent Vector Targeting the Transferrin Receptor: A Novel Application of in Situ Brain Perfusion." *Molecular Pharmaceutics* 11 (1): 243–53. https://doi.org/10.1021/mp400421a.

Ando, Yoshiaki, Hideshi Okada, Genzou Takemura, Kodai Suzuki, Chihiro Takada, Hiroyuki Tomita, Ryogen Zaikokuji, et al. 2018. "Brain-Specific Ultrastructure of Capillary Endothelial Glycocalyx and Its Possible Contribution for Blood Brain Barrier." *Scientific Reports* 8 (1): 17523. https://doi.org/10.1038/s41598-018-35976-2.

Andreone, Benjamin J., Brian Wai Chow, Aleksandra Tata, Baptiste Lacoste, Ayal Ben-Zvi, Kevin Bullock, Amy A. Deik, David D. Ginty, Clary B. Clish, and Chenghua Gu. 2017. "Blood-Brain Barrier Permeability Is Regulated by Lipid Transport-Dependent Suppression of Caveolae-Mediated Transcytosis." *Neuron* 94 (3): 581–94. https://doi.org/10.1016/j.neuron.2017.03.043.

Atwal, Jasvinder K., Yongmei Chen, Cecilia Chiu, Deborah L. Mortensen, William J. Meilandt, Yichin Liu, Christopher E. Heise, et al. 2011. "A Therapeutic Antibody Targeting BACE1 Inhibits Amyloid-β Production in Vivo." *Science Translational Medicine* 3 (84): 84ra43. https://doi.org/10.1126/scitranslmed.3002254.

Ayloo, Swathi, and Chenghua Gu. 2019. "Transcytosis at the Blood–Brain Barrier." *Current Opinion in Neurobiology* 57: 32–38. https://doi.org/10.1016/j.conb.2018.12.014.

Banks, William A., Brie Terrell, Susan A. Farr, Sandra M. Robinson, Naoko Nonaka, and John E. Morley. 2002. "Passage of Amyloid β Protein Antibody across the Blood-Brain Barrier in a Mouse Model of Alzheimer's Disease." *Peptides* 23 (12): 2223–26. https://doi.org/10.1016/S0196-9781(02)00261-9.

Bauer, Hans Christian, István A. Krizbai, Hannelore Bauer, and Andreas Traweger. 2014. "'You Shall Not Pass'-Tight Junctions of the Blood Brain Barrier." *Frontiers in Neuroscience* 8: 1–21. https://doi.org/10.3389/fnins.2014.00392.

Ben-Zvi, Ayal, Baptiste Lacoste, Esther Kur, Benjamin J. Andreone, Yoav Mayshar, Han Yan, and Chenghua Gu. 2014. "Mfsd2a Is Critical for the Formation and Function of the Blood-Brain Barrier." *Nature* 509: 507–11. https://doi.org/10.1038/nature13324.

Bickel, Ulrich. 1995. "Antibody Delivery through the Blood-Brain Barrier." *Advanced Drug Delivery Reviews* 15 (1–3): 53–72. https://doi.org/10.1016/0169-409X(95)00005-R.

Butt, A. M., H. C. Jones, and N. J. Abbott. 1990. "Electrical Resistance across the Blood-brain Barrier in Anaesthetized Rats: A Developmental Study." *The Journal of Physiology* 429 (1): 47–62. https://doi.org/10.1113/jphysiol.1990.sp018243.

Canfield, Scott G., Matthew J. Stebbins, Bethsymarie Soto Morales, Shusaku W. Asai, Gad D. Vatine, Clive N. Svendsen, Sean P. Palecek, and Eric V. Shusta. 2017. "An Isogenic Blood–Brain Barrier Model Comprising Brain Endothelial Cells, Astrocytes, and Neurons Derived from Human Induced Pluripotent Stem Cells." *Journal of Neurochemistry* 140: 874–88. https://doi.org/10.1111/jnc.13923.

Chen, Nancy, Weirong Wang, Scott Fauty, Yulin Fang, Lora Hamuro, Azher Hussain, and Thomayant Prueksaritanont. 2014. "The Effect of the Neonatal Fc Receptor on Human IgG Biodistribution in Mice." *MAbs* 6 (2): 502–8. https://doi.org/10.4161/mabs.27765.

Cilliers, Cornelius, Ian Nessler, Nikolas Christodolu, and Greg M. Thurber. 2017. "Tracking Antibody Distribution with Near-Infrared Fluorescent Dyes: Impact of Dye Structure and Degree of Labeling on Plasma Clearance." *Molecular Pharmaceutics* 14 (5): 1623–33. https://doi.org/10.1021/acs.molpharmaceut.6b01091.

Cooper, Philip R., Gary J. Ciambrone, Connie M. Kliwinski, Eva Maze, Lowell Johnson, Qianqiu Li, Yiqing Feng, and Pamela J. Hornby. 2013. "Efflux of Monoclonal Antibodies from Rat Brain by Neonatal Fc Receptor, FcRn." *Brain Research* 1534: 13–21. https://doi.org/10.1016/j.brainres.2013.08.035.

Daneman, Richard. 2012. "The Blood-Brain Barrier in Health and Disease." *Annals of Neurology* 72 (5): 648–72. https://doi.org/10.1002/ana.23648.

Datta-Mannan, Amita, Jirong Lu, Derrick R. Witcher, Donmienne Leung, Ying Tang, and Victor J. Wroblewski. 2015. "The Interplay of Non-Specific Binding, Targetmediated Clearance and FcRn Interactions on the Pharmacokinetics of Humanized Antibodies." *MAbs* 7 (6): 1084–93. https://doi.org/10.1080/19420862.2015.1075109.

Datta-Mannan, Amita, Arunkumar Thangaraju, Donmienne Leung, Ying Tang, Derrick R. Witcher, Jirong Lu, and Victor J. Wroblewski. 2015. "Balancing Charge in the Complementarity-Determining Regions of Humanized MAbs without Affecting Pl Reduces Non-Specific Binding and Improves the Pharmacokinetics." *MAbs* 7 (3): 483–93. https://doi.org/10.1080/19420862.2015.1016696.

Deane, Rashid, Abhay Sagare, Katie Hamm, Margaret Parisi, Barbra LaRue, Huang

Guo, Zhenhua Wu, David M. Holtzman, and Berislav V. Zlokovic. 2005. "IgG-Assisted Age-Dependent Clearance of Alzheimer's Amyloid β Peptide by the Blood-Brain Barrier Neonatal Fc Receptor." *Journal of Neuroscience* 25 (50): 11495–503. https://doi.org/10.1523/JNEUROSCI.3697-05.2005.

Debie, Pieterjan, and Sophie Hernot. 2019. "Emerging Fluorescent Molecular Tracers to Guide Intra-Operative Surgical Decision-Making." *Frontiers in Pharmacology* 10: 510. https://doi.org/10.3389/fphar.2019.00510.

DeStefano, Jackson G., Zinnia S. Xu, Ashley J. Williams, Nahom Yimam, and Peter C. Searson. 2017. "Effect of Shear Stress on IPSC-Derived Human Brain Microvascular Endothelial Cells (DhBMECs)." *Fluids and Barriers of the CNS* 14 (1): 20. https://doi.org/10.1186/s12987-017-0068-z.

Fan, Jie, Yi Sun, Yifan Xia, John M. Tarbell, and Bingmei M. Fu. 2019. "Endothelial Surface Glycocalyx (ESG) Components and Ultra-Structure Revealed by Stochastic Optical Reconstruction Microscopy (STORM)." *Biorheology* 56 (2–3): 77–88. https://doi.org/10.3233/BIR-180204.

Finke, John M., Kari R. Ayres, Ryan P. Brisbin, Hali A. Hill, Emily E. Wing, and William A. Banks. 2017. "Antibody Blood-Brain Barrier Efflux Is Modulated by Glycan Modification." *Biochimica et Biophysica Acta - General Subjects* 1861 (9): 2228–39. https://doi.org/10.1016/j.bbagen.2017.06.008.

Gabathuler, Reinhard. 2010. "Approaches to Transport Therapeutic Drugs across the Blood-Brain Barrier to Treat Brain Diseases." *Neurobiology of Disease* 37 (1): 48–57. https://doi.org/10.1016/j.nbd.2009.07.028.

Garg, Amit, and Joseph P. Balthasar. 2009. "Investigation of the Influence of FcRn on the Distribution of IgG to the Brain." *AAPS Journal* 11 (3): 553–57. https://doi.org/10.1208/s12248-009-9129-9.

Golde, Todd E. 2014. "Open Questions for Alzheimer's Disease Immunotherapy." *Alzheimer's Research and Therapy* 6: 3. https://doi.org/10.1186/alzrt233.

Golde, Todd E., David R. Borchelt, Benoit I. Giasson, and Jada Lewis. 2013. "Thinking Laterally about Neurodegenerative Proteinopathies." *Journal of Clinical Investigation* 123 (5): 1847–55. https://doi.org/10.1172/JCI66029.

Golde, Todd E., Steven T. DeKosky, and Douglas Galasko. 2018. "Alzheimer's Disease: The Right Drug, the Right Time." *Science* 362 (6420): 1250–51. https://doi.org/10.1126/science.aau0437.

Goulatis, Loukas I., and Eric V. Shusta. 2017. "Protein Engineering Approaches for Regulating Blood–Brain Barrier Transcytosis." *Current Opinion in Structural Biology* 45: 109–15. https://doi.org/10.1016/j.sbi.2016.12.005.

Granath, Kirsti A. 1958. "Solution Properties of Branched Dextrans." *Journal of Colloid Science* 13 (4): 308–28. https://doi.org/10.1016/0095-8522(58)90041-2.

Grevys, Algirdas, Jeannette Nilsen, Kine M.K. Sand, Muluneh B. Daba, Inger Øynebråten, Malin Bern, Martin B. McAdam, et al. 2018. "A Human Endothelial Cell-Based Recycling Assay for Screening of FcRn Targeted Molecules." *Nature Communications* 9: 621. https://doi.org/10.1038/s41467-018-03061-x.

Griffin, D. E., and J. Giffels. 1982. "Study of Protein Characteristics That Influence

Entry into the Cerebrospinal Fluid of Normal Mice and Mice with Encephalitis." *Journal of Clinical Investigation* 70 (2): 289–95. https://doi.org/10.1172/JCI110616.

Grifno, Gabrielle N., Alanna M. Farrell, Raleigh M. Linville, Diego Arevalo, Joo Ho Kim, Luo Gu, and Peter C. Searson. 2019. "Tissue-Engineered Blood-Brain Barrier Models via Directed Differentiation of Human Induced Pluripotent Stem Cells." *Scientific Reports* 9 (1): 13957. https://doi.org/10.1038/s41598-019-50193-1.

Haqqani, Arsalan S., George Thom, Matthew Burrell, Christie E. Delaney, Eric Brunette, Ewa Baumann, Caroline Sodja, Anna Jezierski, Carl Webster, and Danica B. Stanimirovic. 2018. "Intracellular Sorting and Transcytosis of the Rat Transferrin Receptor Antibody OX26 across the Blood–Brain Barrier in Vitro Is Dependent on Its Binding Affinity." *Journal of Neurochemistry* 146 (6): 735–52. https://doi.org/10.1111/jnc.14482.

Hawkins, Brian T., Scott M. Ocheltree, Kristi M. Norwood, and Richard D. Egleton. 2007. "Decreased Blood-Brain Barrier Permeability to Fluorescein in Streptozotocin-Treated Rats." *Neuroscience Letters* 411 (1): 1–5. https://doi.org/10.1016/j.neulet.2006.09.010.

He, Ziyi, Wanling Zhang, Sifeng Mao, Nan Li, Haifang Li, and Jin Ming Lin. 2018. "Shear Stress-Enhanced Internalization of Cell Membrane Proteins Indicated by a Hairpin-Type DNA Probe." *Analytical Chemistry* 90 (9): 5540–45. https://doi.org/10.1021/acs.analchem.8b00755.

Helms, Hans C., N. Joan Abbott, Malgorzata Burek, Romeo Cecchelli, Pierre Olivier Couraud, Maria A. Deli, Carola Förster, et al. 2015. "In Vitro Models of the Blood-Brain Barrier: An Overview of Commonly Used Brain Endothelial Cell Culture Models and Guidelines for Their Use." *Journal of Cerebral Blood Flow and Metabolism* 36 (5): 862–90. https://doi.org/10.1177/0271678X16630991.

Hervé, Françoise, Nicolae Ghinea, and Jean Michel Scherrmann. 2008. "CNS Delivery via Adsorptive Transcytosis." *AAPS Journal* 10 (3): 455–72. https://doi.org/10.1208/s12248-008-9055-2.

Hladky, Stephen B., and Margery A. Barrand. 2018. "Elimination of Substances from the Brain Parenchyma: Efflux via Perivascular Pathways and via the Blood–Brain Barrier." *Fluids and Barriers of the CNS* 15: 30. https://doi.org/10.1186/s12987-018-0113-6.

Hopkins, Amy M., Elise DeSimone, Karolina Chwalek, and David L. Kaplan. 2015. "3D in Vitro Modeling of the Central Nervous System." *Progress in Neurobiology* 125: 1–25. https://doi.org/10.1016/j.pneurobio.2014.11.003.

Howard, Robert, and Kathy Y. Liu. 2020. "Questions EMERGE as Biogen Claims Aducanumab Turnaround." *Nature Reviews Neurology* 16: 63–64. https://doi.org/10.1038/s41582-019-0295-9.

Huang, Yadong, and Lennart Mucke. 2012. "Alzheimer Mechanisms and Therapeutic Strategies." *Cell* 148 (6): 1204–22. https://doi.org/10.1016/j.cell.2012.02.040.

Huynh, John, Nozomi Nishimura, Kuldeepsinh Rana, John M. Peloquin, Joseph P.

Califano, Christine R. Montague, Michael R. King, Chris B. Schaffer, and Cynthia A. Reinhart-King. 2011. "Age-Related Intimal Stiffening Enhances Endothelial Permeability and Leukocyte Transmigration." *Science Translational Medicine* 3 (112): 112–22. https://doi.org/10.1126/scitranslmed.3002761.

Ishikawa, Tomoko, Takami Takizawa, Jun Iwaki, Takuya Mishima, Kumiko Ui-Tei, Toshiyuki Takeshita, Shigeki Matsubara, and Toshihiro Takizawa. 2015. "Fc Gamma Receptor IIb Participates in Maternal IgG Trafficking of Human Placental Endothelial Cells." *International Journal of Molecular Medicine* 35 (5): 1273–89. https://doi.org/10.3892/ijmm.2015.2141.

Joó, Ferenc. 1992. "The Cerebral Microvessels in Culture, an Update." *Journal of Neurochemistry* 58 (1): 1–17. https://doi.org/10.1111/j.1471-4159.1992.tb09272.x.

Kapasi, Alifiya, Charles DeCarli, and Julie A. Schneider. 2017. "Impact of Multiple Pathologies on the Threshold for Clinically Overt Dementia." *Acta Neuropathologica* 134: 171–186. https://doi.org/10.1007/s00401-017-1717-7.

Kaschka, W. P., L. Theilkaes, K. Eickhoff, and F. Skvaril. 1979. "Disproportionate Elevation of the Immunoglobulin G1 Concentration in Cerebrospinal Fluids of Patients with Multiple Sclerosis." *Infection and Immunity* 26 (3): 933–41. https://doi.org/10.1128/iai.26.3.933-941.1979.

Katt, Moriah E., Raleigh M. Linville, Lakyn N. Mayo, Zinnia S. Xu, and Peter C. Searson. 2018. "Functional Brain-Specific Microvessels from IPSC-Derived Human Brain Microvascular Endothelial Cells: The Role of Matrix Composition on Monolayer Formation." *Fluids and Barriers of the CNS* 15 (1): 1–12. https://doi.org/10.1186/s12987-018-0092-7.

Kaufmann, Allyn M., Alana J. Toro-Ramos, and Jeffrey P. Krise. 2008. "Assessment of Golgi Apparatus versus Plasma Membrane-Localized Multi-Drug Resistance-Associated Protein 1." *Molecular Pharmaceutics* 5 (5): 787–94. https://doi.org/10.1021/mp8000205.

Kelly, Ryan L., Yao Yu, Tingwan Sun, Isabelle Caffry, Heather Lynaugh, Michael Brown, Tushar Jain, Yingda Xu, and K. Dane Wittrup. 2016. "Target-Independent Variable Region Mediated Effects on Antibody Clearance Can Be FcRn Independent." *MAbs* 8 (7): 1269–75. https://doi.org/10.1080/19420862.2016.1208330.

Kihara, Takanori, Junri Ito, and Jun Miyake. 2013. "Measurement of Biomolecular Diffusion in Extracellular Matrix Condensed by Fibroblasts Using Fluorescence Correlation Spectroscopy." *PLoS ONE* 8 (11): e82382. https://doi.org/10.1371/journal.pone.0082382.

Kisler, Kassandra, Amy R. Nelson, Axel Montagne, and Berislav V. Zlokovic. 2017. "Cerebral Blood Flow Regulation and Neurovascular Dysfunction in Alzheimer Disease." *Nature Reviews Neuroscience* 18 (7): 419–34. https://doi.org/10.1038/nrn.2017.48.

Kumar, Niyanta N., Michelle E. Pizzo, Geetika Nehra, Brynna Wilken-Resman, Sam Boroumand, and Robert G. Thorne. 2018. "Passive Immunotherapies for Central

Nervous System Disorders: Current Delivery Challenges and New Approaches." *Bioconjugate Chemistry* 29 (12): 3937–66. https://doi.org/10.1021/acs.bioconjchem.8b00548.

Kuo, Timothy T., and Victoria G. Aveson. 2011. "Neonatal Fc Receptor and IgG-Based Therapeutics." *MAbs* 3 (5): 422–30. https://doi.org/10.4161/mabs.3.5.16983.

Kutuzov, Nikolay, Henrik Flyvbjerg, and Martin Lauritzen. 2018. "Contributions of the Glycocalyx, Endothelium, and Extravascular Compartment to the Blood–Brain Barrier." *Proceedings of the National Academy of Sciences of the United States of America* 115 (40): E9429–38. https://doi.org/10.1073/pnas.1802155115.

Lee, Catherine A.A., Hannah S. Seo, Anibal G. Armien, Frank S. Bates, Jakub Tolar, and Samira M. Azarin. 2018. "Modeling and Rescue of Defective Blood-Brain Barrier Function of Induced Brain Microvascular Endothelial Cells from Childhood Cerebral Adrenoleukodystrophy Patients." *Fluids and Barriers of the CNS* 15 (1): 9. https://doi.org/10.1186/s12987-018-0094-5.

Li, Shihong, Jennifer Johnson, Anderson Peck, and Qian Xie. 2017. "Near Infrared Fluorescent Imaging of Brain Tumor with IR780 Dye Incorporated Phospholipid Nanoparticles." *Journal of Translational Medicine* 15: 18. https://doi.org/10.1186/s12967-016-1115-2.

Li, Tengfei, Jean Pierre Bourgeois, Susanna Celli, Fabienne Glacial, Anne Marie Le Sourd, Salah Mecheri, Babette Weksler, et al. 2012. "Cell-Penetrating Anti-GFAP VHH and Corresponding Fluorescent Fusion Protein VHH-GFP Spontaneously Cross the Blood-Brain Barrier and Specifically Recognize Astrocytes: Application to Brain Imaging." *FASEB Journal* 26 (10): 3969–3679. https://doi.org/10.1096/fj.11-201384.

Lippmann, Ethan S., Abraham Al-Ahmad, Samira M. Azarin, Sean P. Palecek, and Eric V. Shusta. 2014. "A Retinoic Acid-Enhanced, Multicellular Human Blood-Brain Barrier Model Derived from Stem Cell Sources." *Scientific Reports* 4: 4160. https://doi.org/10.1038/srep04160.

Long, J.M., and D.M. Holtzman. 2019. "Alzheimer Disease: An Update on Pathobiology and Treatment Strategies." *Cell* 179 (2): 312–39. https://doi.org/10.1016/j.cell.2019.09.001 LK - http://sfx.library.uu.nl/utrecht?sid=EMBASE&issn=10974172&id=doi:10.1016%2Fj.cell.2019.09.001&atitle=Alzheimer+Disease%3A+An+Update+on+Pathobiology+and+Treatment+Strategies&stitle=Cell&title=Cell&volume=179&issue=2&spage=312&epage=339&aulast=Long&aufirst=Justin+M.&auinit=J.M.&aufull=Long+J.M.&coden=CELLB&isbn=&pages=312-339&date=2019&auinit1=J&auinitm=M.

Mantle, Jennifer L., and Kelvin H. Lee. 2019. "Immunoglobulin G Transport Increases in an in Vitro Blood–Brain Barrier Model with Amyloid-β and with Neuroinflammatory Cytokines." *Biotechnology and Bioengineering* 116 (7): 1752–61. https://doi.org/10.1002/bit.26967.

Mantle, Jennifer L., Lie Min, and Kelvin H. Lee. 2016. "Minimum Transendothelial

Electrical Resistance Thresholds for the Study of Small and Large Molecule Drug Transport in a Human in Vitro Blood-Brain Barrier Model." *Molecular Pharmaceutics* 13 (12): 4191–98. https://doi.org/10.1021/acs.molpharmaceut.6b00818.

Montagne, Axel, Daniel A. Nation, Abhay P. Sagare, Giuseppe Barisano, Melanie D. Sweeney, Ararat Chakhoyan, Maricarmen Pachicano, et al. 2020. "APOE4 Leads to Blood–Brain Barrier Dysfunction Predicting Cognitive Decline." *Nature* 581 (7806): 71–76. https://doi.org/10.1038/s41586-020-2247-3.

Neuber, Tobias, Katrin Frese, Jan Jaehrling, Sebastian Jäger, Daniela Daubert, Karin Felderer, Mechthild Linnemann, et al. 2014. "Characterization and Screening of IgG Binding to the Neonatal Fc Receptor." *MAbs* 6 (4): 928–42. https://doi.org/10.4161/mabs.28744.

Niu, Guoguang, Etai Sapoznik, Peng Lu, Tracy Criswell, Aaron M. Mohs, Ge Wang, Sang Jin Lee, Yong Xu, and Shay Soker. 2016. "Fluorescent Imaging of Endothelial Cells in Bioengineered Blood Vessels: The Impact of Crosslinking of the Scaffold." *Journal of Tissue Engineering and Regenerative Medicine* 10 (11): 955–66. https://doi.org/10.1002/term.1876.

Ober, Raimund J., Caius G. Radu, Victor Ghetie, and E. Sally Ward. 2001. "Differences in Promiscuity for Antibody-FcRn Interactions across Species: Implications for Therapeutic Antibodies." *International Immunology* 13 (12): 1551–59. https://doi.org/10.1093/intimm/13.12.1551.

Pardridge, William M. 1998. "Blood-Brain Barrier Carrier-Mediated Transport and Brain Metabolism of Amino Acids." *Neurochemical Research* 23 (5): 635–44. https://doi.org/10.1023/A:1022482604276.

———. 2012. "Drug Transport across the Blood-Brain Barrier." *Journal of Cerebral Blood Flow and Metabolism* 32 (11): 1959–72. https://doi.org/10.1038/jcbfm.2012.126.

———. 2016. "CSF, Blood-Brain Barrier, and Brain Drug Delivery." *Expert Opinion on Drug Delivery* 13 (7): 963–75. https://doi.org/10.1517/17425247.2016.1171315.

———. 2020. "The Isolated Brain Microvessel: A Versatile Experimental Model of the Blood-Brain Barrier." *Frontiers in Physiology* 11: 398. https://doi.org/10.3389/fphys.2020.00398.

Poduslo, Joseph F., Geoffry L. Curran, and Carole T. Berg. 1994. "Macromolecular Permeability across the Blood-Nerve and Blood-Brain Barriers." *Proceedings of the National Academy of Sciences of the United States of America* 91 (12): 5705–9. https://doi.org/10.1073/pnas.91.12.5705.

Pyzik, Michal, Kine M.K. Sand, Jonathan J. Hubbard, Jan Terje Andersen, Inger Sandlie, and Richard S. Blumberg. 2019. "The Neonatal Fc Receptor (FcRn): A Misnomer?" *Frontiers in Immunology* 10: 1540. https://doi.org/10.3389/fimmu.2019.01540.

Qian, Tongcheng, Shaenah E. Maguire, Scott G. Canfield, Xiaoping Bao, William R. Olson, Eric V. Shusta, and Sean P. Palecek. 2017. "Directed Differentiation of

Human Pluripotent Stem Cells to Blood-Brain Barrier Endothelial Cells." *Science Advances* 3: e1701679. https://doi.org/10.1126/sciadv.1701679.

Rhodes, David A., and David A. Isenberg. 2017. "TRIM21 and the Function of Antibodies inside Cells." *Trends in Immunology* 38 (12): 916–26. https://doi.org/10.1016/j.it.2017.07.005.

Ribecco-Lutkiewicz, Maria, Caroline Sodja, Julie Haukenfrers, Arsalan S. Haqqani, Dao Ly, Peter Zachar, Ewa Baumann, et al. 2018. "A Novel Human Induced Pluripotent Stem Cell Blood-Brain Barrier Model: Applicability to Study Antibody-Triggered Receptor-Mediated Transcytosis." *Scientific Reports* 8: 1873. https://doi.org/10.1038/s41598-018-19522-8.

Rouleau, Leonie, Joanna Rossi, and Richard L. Leask. 2010. "Concentration and Time Effects of Dextran Exposure on Endothelial Cell Viability, Attachment, and Inflammatory Marker Expression in Vitro." *Annals of Biomedical Engineering* 38 (4): 1451–62. https://doi.org/10.1007/s10439-010-9934-4.

Ruano-Salguero, John S., and Kelvin H. Lee. 2018. "Efflux Pump Substrates Shuttled to Cytosolic or Vesicular Compartments Exhibit Different Permeability in a Quantitative Human Blood-Brain Barrier Model." *Molecular Pharmaceutics* 15 (11): 5081–88. https://doi.org/10.1021/acs.molpharmaceut.8b00662.

———. 2020. "Antibody Transcytosis across Brain Endothelial-like Cells Occurs Nonspecifically and Independent of FcRn." *Scientific Reports* 10: 3685. https://doi.org/10.1038/s41598-020-60438-z.

Sato, Kazuhide, Tadanobu Nagaya, Yuko Nakamura, Toshiko Harada, Roger R. Nani, James B. Shaum, Alexander P. Gorka, et al. 2015. "Impact of C4′-O-Alkyl Linker on in Vivo Pharmacokinetics of Near-Infrared Cyanine/Monoclonal Antibody Conjugates." *Molecular Pharmaceutics* 12 (9): 3303–11. https://doi.org/10.1021/acs.molpharmaceut.5b00472.

Schlachetzki, Felix, Chunni Zhu, and William M. Pardridge. 2002. "Expression of the Neonatal Fc Receptor (FcRn) at the Blood-Brain Barrier." *Journal of Neurochemistry* 81 (1): 203–6. https://doi.org/10.1046/j.1471-4159.2002.00840.x.

Schneider, Jeffrey R., Ann M. Carias, Arangaserry R. Bastian, Gianguido C. Cianci, Patrick F. Kiser, Ronald S. Veazey, and Thomas J. Hope. 2017. "Long-Term Direct Visualization of Passively Transferred Fluorophore-Conjugated Antibodies." *Journal of Immunological Methods* 450: 66–72. https://doi.org/10.1016/j.jim.2017.07.009.

Seo, Hannah S., Pedram Motallebnejad, and Samira M. Azarin. 2020. "Advances and Opportunities for HiPSC-Derived Models of the Blood-Brain Barrier." *Current Opinion in Chemical Engineering* 30: 1–8. https://doi.org/10.1016/j.coche.2020.05.006.

Sevigny, Jeff, Ping Chiao, Thierry Bussière, Paul H. Weinreb, Leslie Williams, Marcel Maier, Robert Dunstan, et al. 2016. "The Antibody Aducanumab Reduces Aβ Plaques in Alzheimer's Disease." *Nature* 537: 50–56. https://doi.org/10.1038/nature19323.

Shi, Lingyan, Min Zeng, and Bingmei M. Fu. 2014. "Temporal Effects of Vascular Endothelial Growth Factor and 3,5-Cyclic Monophosphate on Blood-Brain Barrier Solute Permeability in Vivo." *Journal of Neuroscience Research* 92 (12): 1678–89. https://doi.org/10.1002/jnr.23457.

Shi, Lingyan, Min Zeng, Yi Sun, and Bingmei M. Fu. 2014. "Quantification of Blood-Brain Barrier Solute Permeability and Brain Transport by Multiphoton Microscopy." *Journal of Biomechanical Engineering* 136 (3): 031005. https://doi.org/10.1115/1.4025892.

Siflinger-Birnboim, Alma, Peter J. del Vecchio, Jeffrey A. Cooper, Frank A. Blumenstock, Jonathan M. Shepard, and Asrar B. Malik. 1987. "Molecular Sieving Characteristics of the Cultured Endothelial Monolayer." *Journal of Cellular Physiology* 132 (1): 111–17. https://doi.org/10.1002/jcp.1041320115.

Soto, Claudio, and Sandra Pritzkow. 2018. "Protein Misfolding, Aggregation, and Conformational Strains in Neurodegenerative Diseases." *Nature Neuroscience* 21 (1332–1340). https://doi.org/10.1038/s41593-018-0235-9.

St-Amour, Isabelle, Isabelle Paré, Wael Alata, Katherine Coulombe, Cassandra Ringuette-Goulet, Janelle Drouin-Ouellet, Milène Vandal, Denis Soulet, Renée Bazin, and Frédéric Calon. 2013. "Brain Bioavailability of Human Intravenous Immunoglobulin and Its Transport through the Murine Blood-Brain Barrier." *Journal of Cerebral Blood Flow and Metabolism* 33 (12): 1983–92. https://doi.org/10.1038/jcbfm.2013.160.

Stalmans, Sofie, Nathalie Bracke, Evelien Wynendaele, Bert Gevaert, Kathelijne Peremans, Christian Burvenich, Ingeborgh Polis, and Bart De Spiegeleer. 2015. "Cell-Penetrating Peptides Selectively Cross the Blood-Brain Barrier in Vivo." *PLoS ONE* 10 (10): e0139652. https://doi.org/10.1371/journal.pone.0139652.

Sun, Haiying, Donald W. Miller, and William F. Elmquist. 2001. "Effect of Probenecid on Fluorescein Transport in the Central Nervous System Using in Vitro and in Vivo Models." *Pharmaceutical Research* 18 (11): 1542–49. https://doi.org/10.1023/A:1013074229576.

Sweeney, Melanie D., Kassandra Kisler, Axel Montagne, Arthur W. Toga, and Berislav V. Zlokovic. 2018. "The Role of Brain Vasculature in Neurodegenerative Disorders." *Nature Neuroscience* 21 (10): 1318–31. https://doi.org/10.1038/s41593-018-0234-x.

The Alzheimer's Association. 2020. "2020 Alzheimer's Disease Facts and Figures." *Alzheimer's and Dementia* 16: 391–460. https://doi.org/10.1002/alz.12068.

Triguero, D., J. L. Buciak, and W. M. Pardridge. 1991. "Cationization of Immunoglobulin G Results in Enhanced Organ Uptake of the Protein after Intravenous Administration in Rats and Primate." *Journal of Pharmacology and Experimental Therapeutics* 258 (1): 186–92.

Uchida, Yasuo, Sumio Ohtsuki, Yuki Katsukura, Chiemi Ikeda, Takashi Suzuki, Junichi Kamiie, and Tetsuya Terasaki. 2011. "Quantitative Targeted Absolute Proteomics of Human Blood-Brain Barrier Transporters and Receptors." *Journal of Neurochemistry* 117 (2): 333–45. https://doi.org/10.1111/j.1471-

4159.2011.07208.x.
Villaseñor, Roberto, Josephine Lampe, Markus Schwaninger, and Ludovic Collin. 2019. "Intracellular Transport and Regulation of Transcytosis across the Blood–Brain Barrier." *Cellular and Molecular Life Sciences* 76 (6): 1081–92. https://doi.org/10.1007/s00018-018-2982-x.
Villasenõr, Roberto, Laurence Ozmen, Nadia Messaddeq, Fiona Grüninger, Hansruedi Loetscher, Annika Keller, Christer Betsholtz, Per Ola Freskgård, and Ludovic Collin. 2016. "Trafficking of Endogenous Immunoglobulins by Endothelial Cells at the Blood-Brain Barrier." *Scientific Reports* 6: 25658. https://doi.org/10.1038/srep25658.
Villaseñor, Roberto, Michael Schilling, Janani Sundaresan, Yves Lutz, and Ludovic Collin. 2017. "Sorting Tubules Regulate Blood-Brain Barrier Transcytosis." *Cell Reports* 21 (11): 3256–70. https://doi.org/10.1016/j.celrep.2017.11.055.
Voigt, Julia, Jon Christensen, and V. Prasad Shastri. 2014. "Differential Uptake of Nanoparticles by Endothelial Cells through Polyelectrolytes with Affinity for Caveolae." *Proceedings of the National Academy of Sciences of the United States of America* 111 (8): 2942–47. https://doi.org/10.1073/pnas.1322356111.
Walsh, Gary. 2018. "Biopharmaceutical Benchmarks 2018." *Nature Biotechnology* 36: 1136–1145. https://doi.org/10.1038/nbt.4305.
Wang, Qin, Luisette Delva, Paul H. Weinreb, Robert B. Pepinsky, Danielle Graham, Elvana Veizaj, Anne E. Cheung, et al. 2018. "Monoclonal Antibody Exposure in Rat and Cynomolgus Monkey Cerebrospinal Fluid Following Systemic Administration." *Fluids and Barriers of the CNS* 15 (1): 10. https://doi.org/10.1186/s12987-018-0093-6.
Ward, E. Sally, and Raimund J. Ober. 2018. "Targeting FcRn to Generate Antibody-Based Therapeutics." *Trends in Pharmacological Sciences* 39 (10): 892–904. https://doi.org/10.1016/j.tips.2018.07.007.
Ward, E. Sally, Jinchun Zhou, Victor Ghetie, and Raimund J. Ober. 2003. "Evidence to Support the Cellular Mechanism Involved in Serum IgG Homeostasis in Humans." *International Immunology* 13: 1551–59. https://doi.org/10.1093/intimm/dxg018.
Warren, Mark S., Noa Zerangue, Katie Woodford, Lori M. Roberts, Emily H. Tate, Bo Feng, Cheryl Li, et al. 2009. "Comparative Gene Expression Profiles of ABC Transporters in Brain Microvessel Endothelial Cells and Brain in Five Species Including Human." *Pharmacological Research* 59 (6): 404–13. https://doi.org/10.1016/j.phrs.2009.02.007.
Watts, Ryan J., and Mark S. Dennis. 2013. "Bispecific Antibodies for Delivery into the Brain." *Current Opinion in Chemical Biology* 17 (3): 393–99. https://doi.org/10.1016/j.cbpa.2013.03.023.
Weber, Felix, Bernd Bohrmann, Jens Niewoehner, Jens A.A. Fischer, Petra Rueger, Georg Tiefenthaler, Joerg Moelleken, et al. 2018. "Brain Shuttle Antibody for Alzheimer's Disease with Attenuated Peripheral Effector Function Due to an Inverted Binding Mode." *Cell Reports* 22 (1): 149–62.

https://doi.org/10.1016/j.celrep.2017.12.019.
Wen, Xiangyi, Grant W. Saltzgaber, and Wallace B. Thoreson. 2017. "Kiss-and-Run Is a Significant Contributor to Synaptic Exocytosis and Endocytosis in Photoreceptors." *Frontiers in Cellular Neuroscience* 11: 286. https://doi.org/10.3389/fncel.2017.00286.
Wilson, Hannah K., Scott G. Canfield, Michael K. Hjortness, Sean P. Palecek, and Eric V. Shusta. 2015. "Exploring the Effects of Cell Seeding Density on the Differentiation of Human Pluripotent Stem Cells to Brain Microvascular Endothelial Cells." *Fluids and Barriers of the CNS* 12: 13. https://doi.org/10.1186/s12987-015-0007-9.
Workman, Michael J., and Clive N. Svendsen. 2020. "Recent Advances in Human IPSC-Derived Models of the Blood-Brain Barrier." *Fluids and Barriers of the CNS* 17 (1): 30. https://doi.org/10.1186/s12987-020-00191-7.
Wuest, Diane M., and Kelvin H. Lee. 2012. "Optimization of Endothelial Cell Growth in a Murine in Vitro Blood-Brain Barrier Model." *Biotechnology Journal* 7 (3): 409–17. https://doi.org/10.1002/biot.201100189.
Wuest, Diane M., Allison M. Wing, and Kelvin H. Lee. 2013. "Membrane Configuration Optimization for a Murine in Vitro Blood-Brain Barrier Model." *Journal of Neuroscience Methods* 212 (2): 211–21. https://doi.org/10.1016/j.jneumeth.2012.10.016.
Yanagida, Keisuke, Catherine H. Liu, Giuseppe Faraco, Sylvain Galvani, Helen K. Smith, Nathalie Burg, Josef Anrather, Teresa Sanchez, Costantino Iadecola, and Timothy Hla. 2017. "Size-Selective Opening of the Blood-Brain Barrier by Targeting Endothelial Sphingosine 1-Phosphate Receptor 1." *Proceedings of the National Academy of Sciences of the United States of America* 114 (17): 4531–36. https://doi.org/10.1073/pnas.1618659114.
Yang, Andrew C., Marc Y. Stevens, Michelle B. Chen, Davis P. Lee, Daniel Stähli, David Gate, Kévin Contrepois, et al. 2020. "Physiological Blood–Brain Transport Is Impaired with Age by a Shift in Transcytosis." *Nature* 583 (7816): 425–30. https://doi.org/10.1038/s41586-020-2453-z.
Yang, Ya Li, Lindsay M. Leone, and Laura J. Kaufman. 2009. "Elastic Moduli of Collagen Gels Can Be Predicted from Two-Dimensional Confocal Microscopy." *Biophysical Journal* 97: 2051–60. https://doi.org/10.1016/j.bpj.2009.07.035.
Yip, Victor, Enzo Palma, Devin B. Tesar, Eduardo E. Mundo, Daniela Bumbaca, Elizabeth K. Torres, Noe A. Reyes, et al. 2014. "Quantitative Cumulative Biodistribution of Antibodies in Mice: Effect of Modulating Binding Affinity to the Neonatal Fc Receptor." *MAbs* 6 (3): 689–96. https://doi.org/10.4161/mabs.28254.
Yu, Y. Joy, Jasvinder K. Atwal, Yin Zhang, Raymond K. Tong, Kristin R. Wildsmith, Christine Tan, Nga Bien-Ly, et al. 2014. "Therapeutic Bispecific Antibodies Cross the Blood-Brain Barrier in Nonhuman Primates." *Science Translational Medicine* 6 (261): 261ra154. https://doi.org/10.1126/scitranslmed.3009835.
Yu, Y. Joy, and Ryan J. Watts. 2013. "Developing Therapeutic Antibodies for

Neurodegenerative Disease." *Neurotherapeutics* 10 (3): 459–72. https://doi.org/10.1007/s13311-013-0187-4.

Zeng, Ye, Eno E. Ebong, Bingmei M. Fu, and John M. Tarbell. 2012. "The Structural Stability of the Endothelial Glycocalyx after Enzymatic Removal of Glycosaminoglycans." *PLoS ONE* 7 (8): e43168. https://doi.org/10.1371/journal.pone.0043168.

Zhao, Zhen, Amy R. Nelson, Christer Betsholtz, and Berislav V. Zlokovic. 2015. "Establishment and Dysfunction of the Blood-Brain Barrier." *Cell* 163 (5): 1064–78. https://doi.org/10.1016/j.cell.2015.10.067.

Zlokovic, B. V., D. S. Skundric, M. B. Segal, M. N. Lipovac, J. B. Mackic, and H. Davson. 1990. "A Saturable Mechanism for Transport of Immunoglobulin G across the Blood-Brain Barrier of the Guinea Pig." *Experimental Neurology* 107 (3): 263–70. https://doi.org/10.1016/0014-4886(90)90144-H.

Appendix A

SUPPLEMENTARY INFORMATION FOR CHAPTER 2

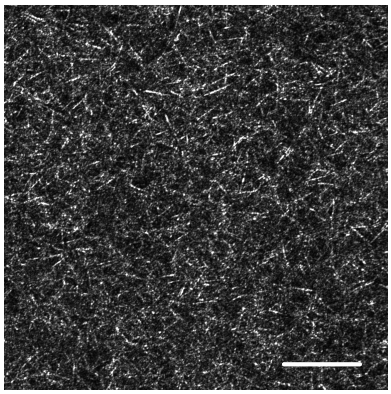

Figure A-1: Representative confocal reflection microscopy image of a 5 mg/mL COL1 hydrogel formed at 37 ºC. Scale bar is 20 µm.

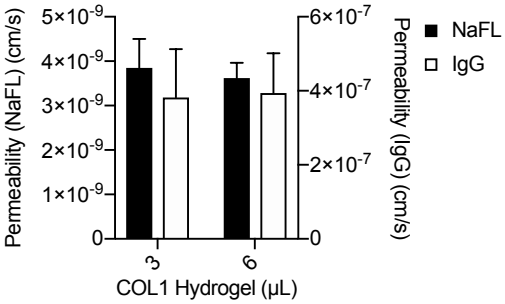

Figure A-2: NaFL and IgG permeability of hiPSC-BMECs grown on COL1 hydrogels of 3 or 6 µL. Statistical significance was determined using a Student's t test. Values are mean ± SEM of four individual hydrogels from two independent differentiations.

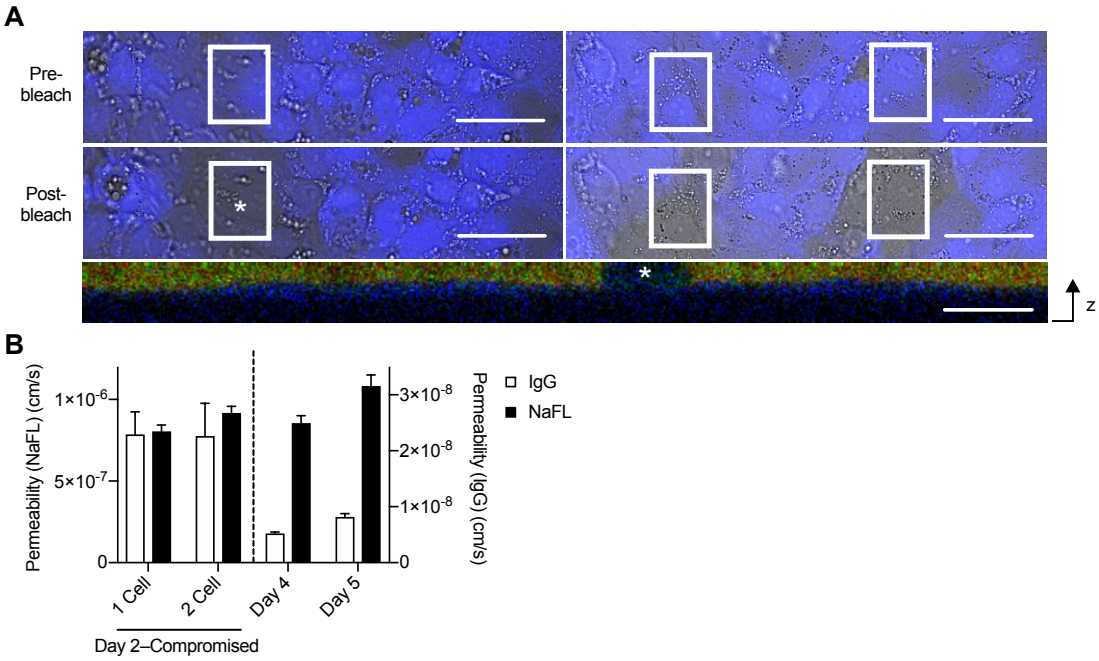

Figure A-3: Analysis of NaFL and IgG permeability following photobleaching of hiPSC-BMEC monolayers using confocal microscopy. (A) A comparison of hiPSC-BMEC monolayers, positive for live-cell CB blue staining (blue), before (Pre-bleach) and after (Post-bleach) the photobleaching of one (left) or two (right) regions (white boxes). Figures are composite fluorescent and brightfield (greyscale) images. Scale bar is 40 µm. A vertical profile of Post-bleach cells with one photobleached region is shown in the bottom panel, where NaFL (green) and IgG (red) help identify the rounded, CB-negative compromised cell (indicated with a *). Scale bar is 20 µm. (B) Permeability values of compromised monolayers and Day 4 and Day 5 uncompromised monolayers. Statistical significance was determined using a Student's t test. Values are mean ± SEM of four individual hydrogels from two independent differentiations.

Appendix B

SUPPLEMENTARY INFORMATION FOR CHAPTER 3

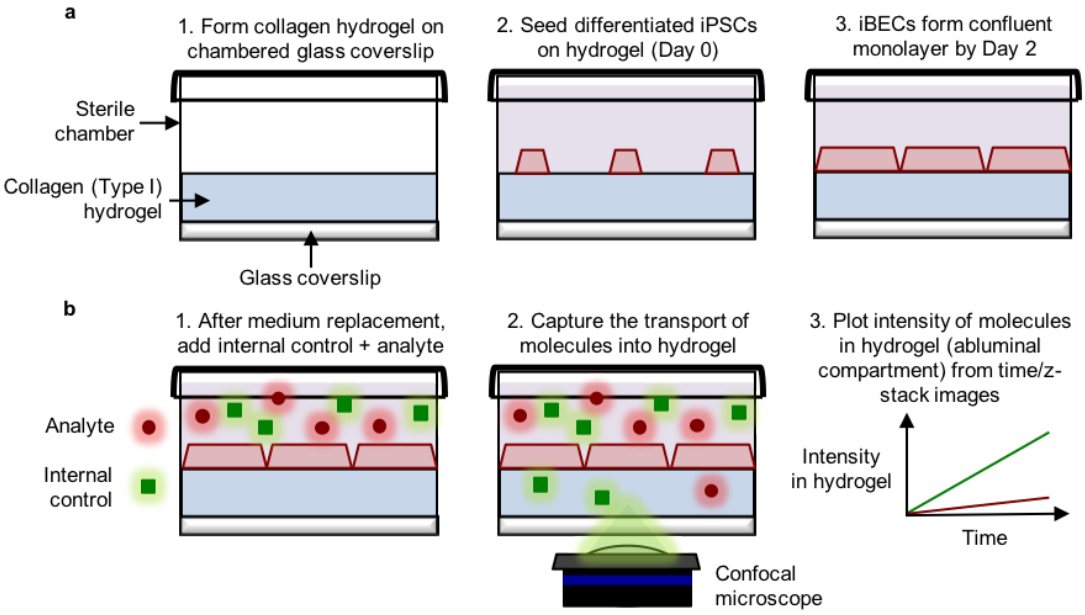

Figure B-1: Illustration of hydrogel-based BBB model. (**a**) Procedure to form a confluent iBEC monolayer on a collagen type I hydrogel. (**b**) Measurement and analysis of monolayer permeability.

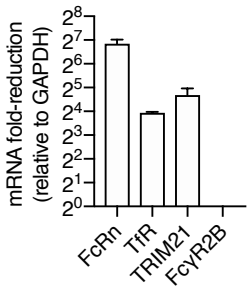

Figure B-2: Evaluation of gene expression by qRT-PCR. Levels of mRNA for each gene are shown relative to GAPDH (reference gene). Values are from three independent differentiations, run in technical triplicate, ± SEM.

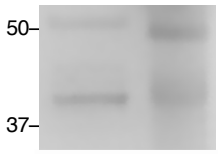

Figure B-3: Protein expression of FcRn by western analysis. The left lane is purified human FcRn (biotinylated) and the right lane is iBEC lysate.

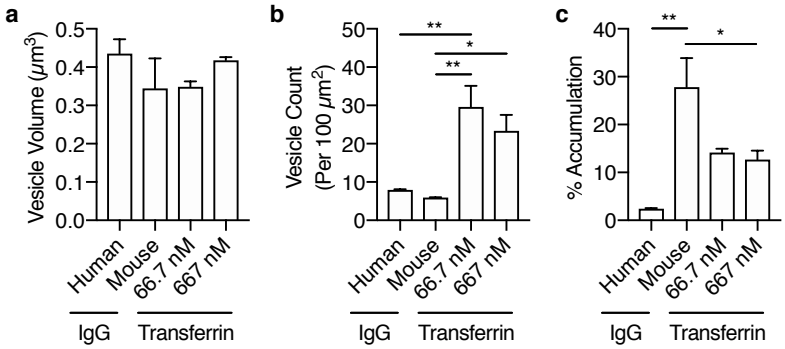

Figure B-4: Differential intracellular processing of IgG and transferrin by iBECs after 1 hour. (**a**) Volume and (**b**) number of vesicles containing fluorescently-labeled macromolecules. (**c**) Quantification of average vesicle intensity relative to inoculum intensity. Values represent the means from three independent differentiations ± SEM, where each value is an average from five 192 × 192 μm^2 images. Means were compared using one-way ANOVA followed by Tukey's multiple comparison test (*P < 0.05, **P < 0.01).

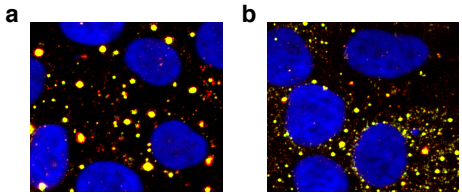

Figure B-5: Visualization of LAMP2 colocalization in iBECs after 1 hour. Representative deconvolved Airyscan super-resolution confocal images showing the intracellular vesicular structures containing fluorescently-labeled (**a**) human or (**b**) mouse IgG (green) and LAMP2-positive lysosomes (red). Images are Z-projections based on average intensity, nucleus is stained with DAPI (blue), and scale bar represents 10 μm.

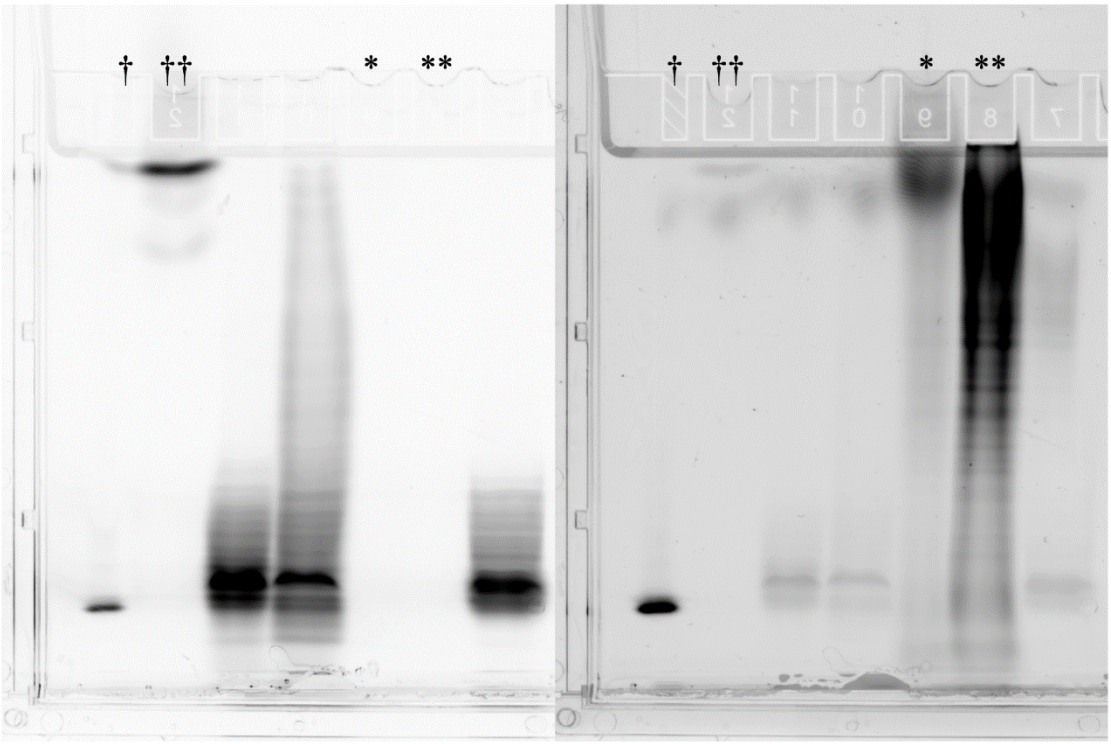

Figure B-6: Fluorescent images of a single IEF gel. The excitation/emission wavelengths were 635/670 nm (left) and 532/580 nm (right). The IEF standard is denoted †, the sdAb is denoted ††, and the 10-kDa and 155-kDa dextrans are denoted * and **, respectively.

Appendix C

SUPPLEMENTARY INFORMATION FOR Chapter 4

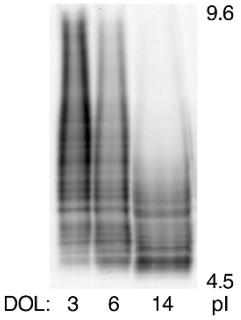

Figure C-1: Isoelectric focusing gel. Sulfo-Cy5 signal from IgG conjugates demonstrating a decreasing isoelectric point (pI) with increasing degree of labeling (DOL).

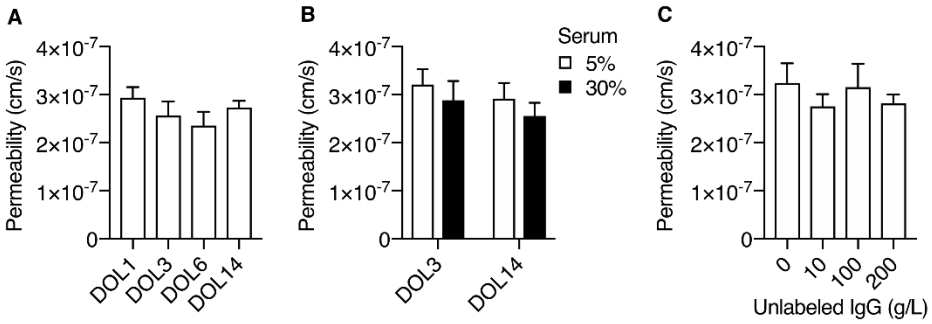

Figure C-2: Paracellular permeability internal control. Corresponding permeability of sodium fluorescein for Figure 4-1(A), Figure 4-2(B), and Figure 4-2(C).

Appendix D

PERMISSIONS FOR REPRINT

Chapter 2 reprinted with permission from:

Ruano-Salguero JR, Lee KH. 2018. Efflux pump substrates shuttled to cytosolic or vesicular compartments exhibit different permeability in a quantitative human blood–brain barrier model. Molecular Pharmaceutics 15:5081-5088

ACS Publications
Most Trusted. Most Cited. Most Read.

Efflux Pump Substrates Shuttled to Cytosolic or Vesicular Compartments Exhibit Different Permeability in a Quantitative Human Blood–Brain Barrier Model

Author: John S. Ruano-Salguero, Kelvin H. Lee

Publication: Molecular Pharmaceutics

Publisher: American Chemical Society

Date: Nov 1, 2018

Copyright © 2018, American Chemical Society

PERMISSION/LICENSE IS GRANTED FOR YOUR ORDER AT NO CHARGE

This type of permission/license, instead of the standard Terms & Conditions, is sent to you because no fee is being charged for your order. Please note the following:

- Permission is granted for your request in both print and electronic formats, and translations.
- If figures and/or tables were requested, they may be adapted or used in part.
- Please print this page for your records and send a copy of it to your publisher/graduate school.
- Appropriate credit for the requested material should be given as follows: "Reprinted (adapted) with permission from (COMPLETE REFERENCE CITATION). Copyright (YEAR) American Chemical Society." Insert appropriate information in place of the capitalized words.
- One-time permission is granted only for the use specified in your request. No additional uses are granted (such as derivative works or other editions). For any other uses, please submit a new request.

BACK CLOSE WINDOW

Chapter 3 reprinted with permission from:

Ruano-Salguero JR, Lee KH. 2020. Antibody transcytosis across brain endothelial-like cells occurs nonspecifically and independent of FcRn. Scientific Reports 10:3685 doi.org/10.1038/s41598-020-60438-z

Chapter 4 was reproduced with permission from Molecular Pharmaceutics, in press. Unpublished work copyright 2020 American Chemical Society.